frontiers | Frontiers in Environmental Science

TYPE Original Research
PUBLISHED 22 November 2024
DOI 10.3389/fenvs.2024.1474742

OPEN ACCESS

EDITED BY
Bushra Khalid,
Chinese Academy of Sciences (CAS), China

REVIEWED BY
Faustin Katchele Ogou,
Chinese Academy of Sciences (CAS), China
Muhammad Luqman,
Australian Institute of Health and Welfare, Australia

*CORRESPONDENCE
Prabuddh Kumar Mishra,
prabuddh@shivaji.du.ac.in

RECEIVED 02 August 2024
ACCEPTED 11 November 2024
PUBLISHED 22 November 2024

CITATION
Chanuwan Wijesinghe D, Withanage NC, Mishra PK, Frenando WS, Abdelrahman K and Fnais MS (2024) The impacts of landscape structure changes on urban surface temperature and heat islands formation of a growing city in southern Sri Lanka. *Front. Environ. Sci.* 12:1474742. doi: 10.3389/fenvs.2024.1474742

The impacts of landscape structure changes on urban surface temperature and heat islands formation of a growing city in southern Sri Lanka

Dilnu Chanuwan Wijesinghe[1,2], Neel Chaminda Withanage[1,2], Prabuddh Kumar Mishra[3]*, Wasana Surandi Frenando[2], Kamal Abdelrahman[4] and Mohammed S. Fnais[4]

[1]School of Geographical Sciences, Southwest University, Chongqing, China, [2]Department of Geography, Faculty of Humanities and Social Sciences, University of Ruhuna, Matara, Sri Lanka, [3]Department of Geography, Shivaji College, University of Delhi, New Delhi, India, [4]Department of Geology and Geophysics, College of Science, King Saud University, Riyadh, Saudi Arabia

Undoubtedly, urbanization has improved human living conditions. However, it has also altered the natural landscape, leading to negative consequences such as increased Land Surface Temperature (LST) and Urban Heat Island (UHI) due to the expansion of Impervious Surface (IS). Much research has been conducted in other countries on the effects of changing urban landscape structures on LST and UHI formation. However, in Sri Lanka, only a few studies have been available on this topic, primarily concentrating on major cities like Colombo. Impervious Surface is absorbing high amounts of solar energy as well, which accelerates the magnitude of UHI in urbanized areas. Remote Sensing indices such as the Normalized Difference Vegetation Index (NDVI), Normalized Difference Buildup Index (NDBI), UHI, and Environmental Criticality Index (ECI) can effectively be used to quantify the intensity of the UHI phenomenon. This study aimed to investigate the effect of spatiotemporal variations in IS and Green Surface (GS) on UHI, LST, and the environmental criticality in Galle Municipal Council (MC), Sri Lanka employing multi-temporal Landsat-5 and 8 data from four different periods: 1996, 2005, 2014, and 2022. Different geospatial techniques including supervised image classification, Urban-Rural Gradient Zone (URGZ) analysis, grid-based analysis, UHI profiles, and regression analysis were used in the study. The findings revealed that Impervious Surface increased by 42.3% (7.34 km^2) while Green Surface had a decline of 22.5% (3.91 km^2) during the concerned period. This landscape transition led to a 2.74 C increase in mean surface temperature in the study area, along with a 9.5 C increase in the UHI index during 26 years. The results further revealed that Impervious Surface rapidly developed within 4 km (URGZ1-19) from city center, while Green Surface decreased. Newly built-up areas within the 1.5 km gradient (URGZ1-URGZ8) were more affected by increased LST. A positive correlation was identified between NDBI and LST, especially in the year 2022, with an R^2 of 0.457, while NDVI and LST reported a negative R^2 of 0.257. The grid-based analysis demonstrated an increasingly positive relationship between mean LST and the fraction of Impervious Surface, highlighting the role of built-up areas in raising LST and UHI in the MC. As a result, very high environmental critical areas have been concentrated in and around high-density Impervious Surface. Thus, it can be predicted that the UHI effect and

Environmental Criticality (EC) may increase further in the future. In this context, planning agencies should prioritize green urban planning strategies, such as implementing green belts and urban agriculture in the study area, particularly in and around areas with high LST and high environmental criticality. This approach may help protect the natural environment and sustainably ensure the health of the urban community.

KEYWORDS

ECI, Galle, green surface, UHI, urbanization, impervious surface, landscape, LST

1 Introduction

In recent years, urbanization has intensified, emerging as a major global spatial phenomenon (Withanage N. C. et al., 2023; Withanage et al., 2024; Withanage and Jingwei, 2024). Urbanization levels can range from micro-scale administrative areas to broader geographical regions (Pannell, 2002). In 2018, 55% of the global population resided in cities, with projections indicating a rise to 68% by 2050 United Nations, Department of Economic and Social Affairs, Population Division (2019). In developing countries worldwide, migration from rural areas and urban infrastructure development continue to attract populations toward cities. Rapid growth of population is a predominant factor in the acceleration of the urbanization process in developing countries due to the functioning of the "push and pull" factors. This process leads to the growth of industrialization, transportation, and infrastructure development, as well as an increase in natural resource utilization in urban areas. This multidimensional process is reshapes socio-economic activities and alters the spatial distribution of Green Surface (GS) and Impervious Surface (IS) (United Nations, Department of Economic and Social Affairs, Population Division, 2019). Impervious surface refers to areas with high levels of built-up coverage, typically including buildings, roads, and other infrastructure.

Urban areas are frequently thought of as impervious areas that are covered by roads, buildings, and other constructed structures (Withanage N. C. et al., 2023). Rapid landscape transformations, including the conversion of green surface and agricultural land into impervious surface, have introduced various challenges. These issues span multiple scales, affecting farmland fragmentation, habitat loss, and air, water, and soil pollution, alongside the spread of vector-borne diseases and rising Land Surface Temperature (LST) (Deng et al., 2016; Ho et al., 2016; Son et al., 2017; Hou et al., 2019; Ranagalage et al., 2019). Presently, scholars have identified that impervious surface changes are compatible with variations in urban LST, and that leads to the formation of UHI (Ranagalage et al., 2019; Ranagalage et al., 2020).

UHI is a significant environmental issue that adversely affects the natural environment and human health. UHI is a phenomenon that comprises high thermal temperatures in IS compared with other areas. Surface UHI and atmospheric UHI are the major categories of UHI (Environmental Protection Agency, 2008). The extensive growth of construction and the expansion of IS have contributed to the rise in LST and the intensification of the UHI effect in urban areas. The intensity of UHI has been influenced by the rising temperature between 2 and 8°C within the IS (Silva et al., 2018). Thus, Green urban planning is an essential and effective strategy for mitigating the adverse impact of UHI since adverse impacts of UHI have been propagated in the recent past. Therefore, systematic investigations of UHI using remote sensing (RS) data and techniques, integrated with geographical information systems (GIS), have been significantly increasing.

Geospatial technology allows for optimal decision-making by integrating geographical data models across spatial and temporal dimensions (Withanage et al., 2024; Jayasinghe and Withanage, 2020; Wimalasena and Withanage, 2022; Withanage W. K. et al., 2023; Wijesinghe et al., 2023; Nuwanka and Withanage, 2024; Withanage et al., 2024). RS data is very important and reliable source for examining the structural changes of IS and its effects on the UHI (Weng, 2002). Advancements in RS technology have made it possible to obtain thermal and optical data from the same sensor platforms, which is beneficial for researching temperature conditions and changes in Impervious Surface (Choe and Yom, 2020). Due to the lack of meteorological data, especially in developing countries, RS methods have become an effective and reliable source for UHI and LST assessment (Jain et al., 2020; Teferi and Abraha, 2017; Ranagalage et al., 2019; Wijesinghe et al., 2024). Satellite images with different time scales have provided an opportunity to examine the magnitude of UHI in IS. High-resolution satellite data such as National Oceanic and Atmospheric Administration (NOAA), and Moderate Resolution Imaging Spectroradiometer (MODIS) are highly appropriate for examining the mass-scale impacts of air temperature as well moderate-resolution satellite images such as Landsat and ASTER are also fine for the analysis of LST and UHI (Weng, 2009; Cheng et al., 2022; Priyankara et al., 2019). Nighttime light data, and Synthetic Aperture Radar (SAR) data have also been utilized in previous studies to assess urban LST and the UHI effect (Marconcini et al., 2014; Paranunzio et al., 2019).

There has been a wide range of scholarly studies on the Landscape dynamics contribution of UHI incorporating RS in the recent past (Santos et al., 2017; Bokaie et al., 2019; Dissanayake et al., 2019; Fonseka et al., 2019; Ranagalage et al., 2017; Estoque et al., 2017). These studies widely focus on how Land Use/Land Cover (LULC) changes have led to the enhancement of the severity of UHI in developing countries. An analysis of Landsat images from 2011 to 2019 revealed a 1.86 C increase in LST in Narayanganj City, Bangladesh (Rishid et al., 2022). Furthermore, a significant correlation was observed between LST and the Normalized Differences Built-up Index (NDBI) (Rashid et al., 2022). LULC changes have led to the growth of LST between 6.05 C from 2007 to 2020 in Wuhan City, China due to the expansion of buildup areas (Cheng et al., 2022; Wanga et al., 2019). Using Landsat TM/ETM+/OLI-TIRS images another study

was conducted in Yerevan city which was in Armenia (Tepanosyan et al., 2021). That study also pointed out that the decline of LULC caused an increase in the impact of UHI (Tepanosyan et al., 2021). Normalized Differences Vegetation Index (NDVI) and NDBI were calculated using Landsat images from 2005 to 2019 in Kolkata and found that LST had rapidly increased within the urban core due to the increase of the IS over GS (Chatterjee and Majumdar, 2022). In addition, a recent study focused on the space-borne sensor data set using the Multifractal Detrended Fluctuation Analysis (MDFA) in the Indian Himalayan foothills. That study also confirmed that the urbanization process accelerated the UHI (Kimothi et al., 2023).

In the Sri Lankan context, several studies can be identified on how the urbanization process and the structural transformation of the IS affect variations of LST in cities (Ranagalage et al., 2017; Dissanayake al., 2019; Ranagalage et al., 2019). Expansion of the Colombo urban area and urban density positively impacted the LST during 1988–2016 (Fonseka et al., 2019). Landsat 7 ETM + data in 2000–2001 was utilized to identify the correlation between the LU/LC and LST distribution pattern in Colombo and they stated that the UHI is significant in the port area (Senanayake et al., 2013; Ranagalage et al., 2017). A few scholars have investigated changes in landscape structure and UHI and their influences on the ecology and socio-economic environment in peripheral urban areas such as Gampola, and Nuwara Eliya apart from capital (Ranagalage et al., 2019; Ranagalage et al., 2020; Arachchi, 2022).

Southern province is the 7th largest province, and it provides residence for 2.5 million inhabitants (Kumara, 2022). Urbanization and growing population density have led to the change of IS in this area compared to the previous decades (Dissanayake, 2020). The Galle MC was chosen as the study area due to its status as the fourth largest municipality in Sri Lanka and its strategic connection to other main cities such as Matara and Kalutara via the A2 road. Urbanization and commuting over the past two decades have led to a significant influx of population into the study area, which is a popular tourist destination and port city. Only one previous study is available in the study area that investigated LULC changes in LST and UHI effects (Dissanayake, 2020). However, there is a gap as the previous study did not extensively explore the relationship between Impervious Surface expansion, LST, UHI effects along URGZ, and the measurement of environmental criticality (EC). We attempted to address this gap by evaluating the correlation between landscape dynamics and UHI considering the distance effect from the city center using URGZ and grid-based analysis. Also, our study emphasizes the Environmental Criticality (EC) associated with the expansion of Impervious Surface with decreasing Green Surface. The findings of the study will assist in sustainable urban planning and help reduce the impacts of landscape changes in the Galle MC, thereby safeguarding the environment and securing human health.

2 Materials and methods

2.1 Study area

The coastal city of Galle, the capital of the southern province, of Sri Lanka is bounded to the south and southwest by the Indian Ocean which is located in 6°.10′ north latitude and 80°.13′ east longitude. It serves as both the district and provincial capital and is regarded as the largest city in the Southern Province. Since the southern province is home to the primary business hub, Galle is a bustling city where many inheritances live and work (UDA, 2019). In the study, Galle MC (Figure 1) was selected and it lies within the wet zone with an average temperature of 28–30°C and 1,525–1900 mm average rainfall. Except for a few isolated peaks of about 60–160 feet, other areas consist of flat terrain. Also, from the agro-climatological perspective, the MC belongs to the wet zone (Dissanayake, 2020). Especially, Galle is the third municipal council in Sri Lanka, founded following the terms of the urban council statute of 1865 (Abeyweera and Kaluthanthri, 2018). In 1988, Galle City was named a World Heritage City in Sri Lanka by the United Nations.

2.2 Description of data and preprocessing

The Landsat satellite images with a minimum cloud cover of less than 5% or without any clouds during the wet and dry seasons were downloaded via the United States Geological Survey (USGS) website (USGS, Accessed on 12 November 2023). All images were projected into WGS84/UTM 44N to maintain spatial consistency. The whole study area belongs to path 56 and row 141. The summary of all the data in the two sensors is included in Table 1.

To establish a thorough link between the acquired data and the biophysical properties of the landscape, preprocessing must be done before image classification and change detection (Land-resources, 2023). The identification of minute variations in surface reflectance and LULC is necessary for this investigation. The thermal bands (TM band 6 and OLI band 10) were employed for the retrieval of LST after radiation and atmospheric corrections (Landsat 8 (L8), 2016). To process and analyze the data, Arc Map 10.8 (ESRI, 2020), MS Office Excel (Microsoft, 1988), and Origin Pro data analysis and graphing software (Origin Lab Corporation, 2023, MA, United States) were used.

2.3 Methods

Several steps were followed to create LU/LC maps including image preprocessing, classification, accuracy checking, and change detection. Retrieval of NDVI, NDBI, NDWI, LST, UHI, and ECI was performed using standardized equations. The technical flowchart explaining the combination of image preprocessing, image classification, retrieval of RS-based indices, and other geospatial and statistical analysis is presented in Figure 2.

2.3.1 LULC classification

Both LULCs are considerably described by land-use categorization. To promote sustainable development, policymakers can better grasp the dynamics of environmental change by LULC mapping (Kennedy et al., 2018; Cabral et al., 2016). Due to spectral heterogeneity, categorizing satellite images of urban areas is considered a complicated operation. Past researchers have classified satellite image pixels into different classes through various approaches (Wang et al., 2019; Rimal et al., 2017). For LULC analysis purposes, we classified Landsat images in the years 1996,

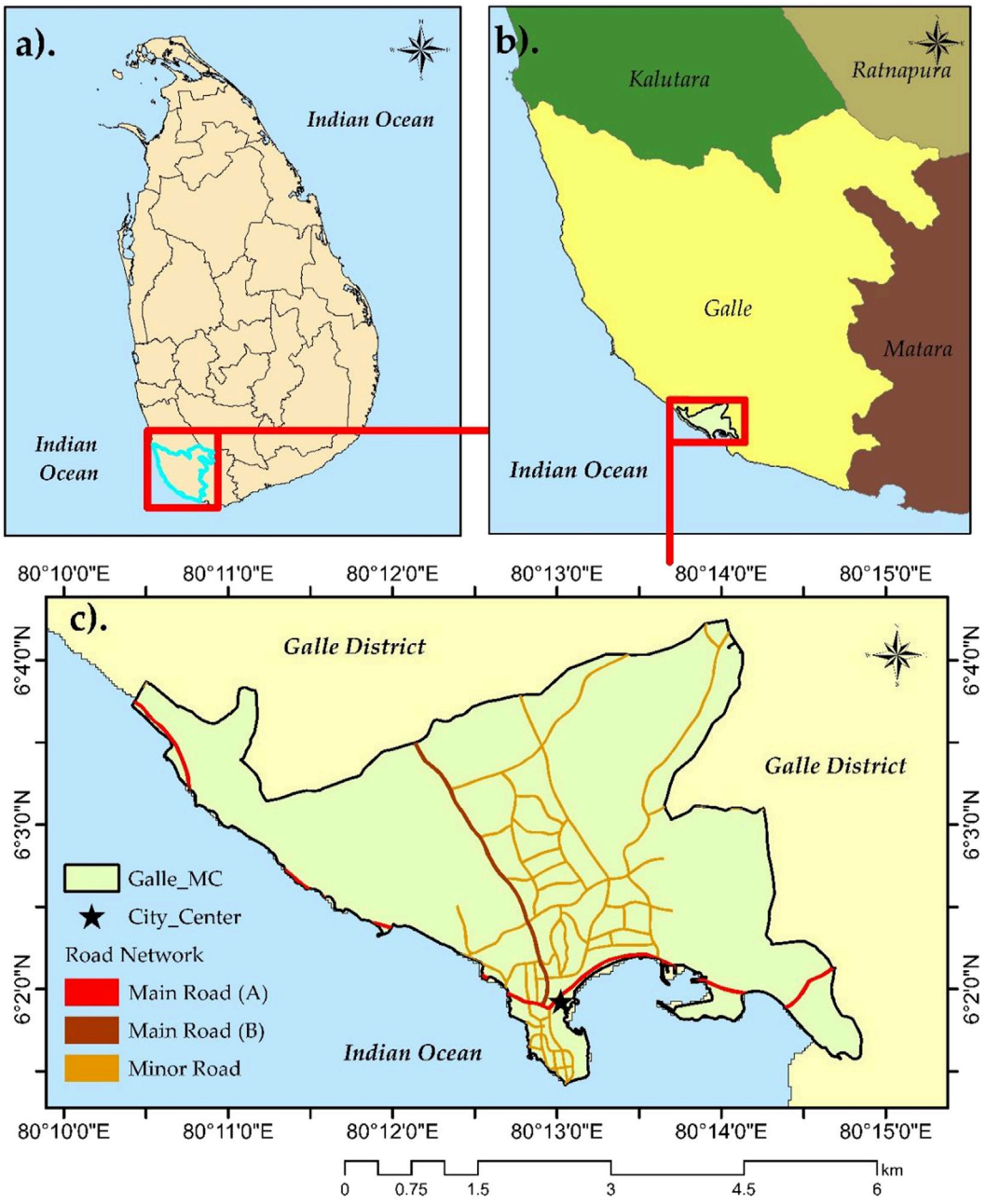

FIGURE 1
Location: **(A)** Galle district in Sri Lanka **(B, C)** Galle MC area.

TABLE 1 Description of the Satellite Datasets.

Satellite	Path/Row	Date	Time (GMT)	Cloud cover	Thermal conversion constants	
					K_1	K_2
Landsat 5 TM	141/056	24/03/1996	04:02:02	2.00	607.76	1,260.56
Landsat 5 TM	141/056	13/02/2005	04:40:37	1.00	607.76	1,260.56
Landsat 8 OLI	141/056	10/03/2014	04:54:36	3.27	774.8853	1,321.0789
Landsat 8 OLI	141/056	26/01/2022	04:02:02	4.11	774.8853	1,321.0789

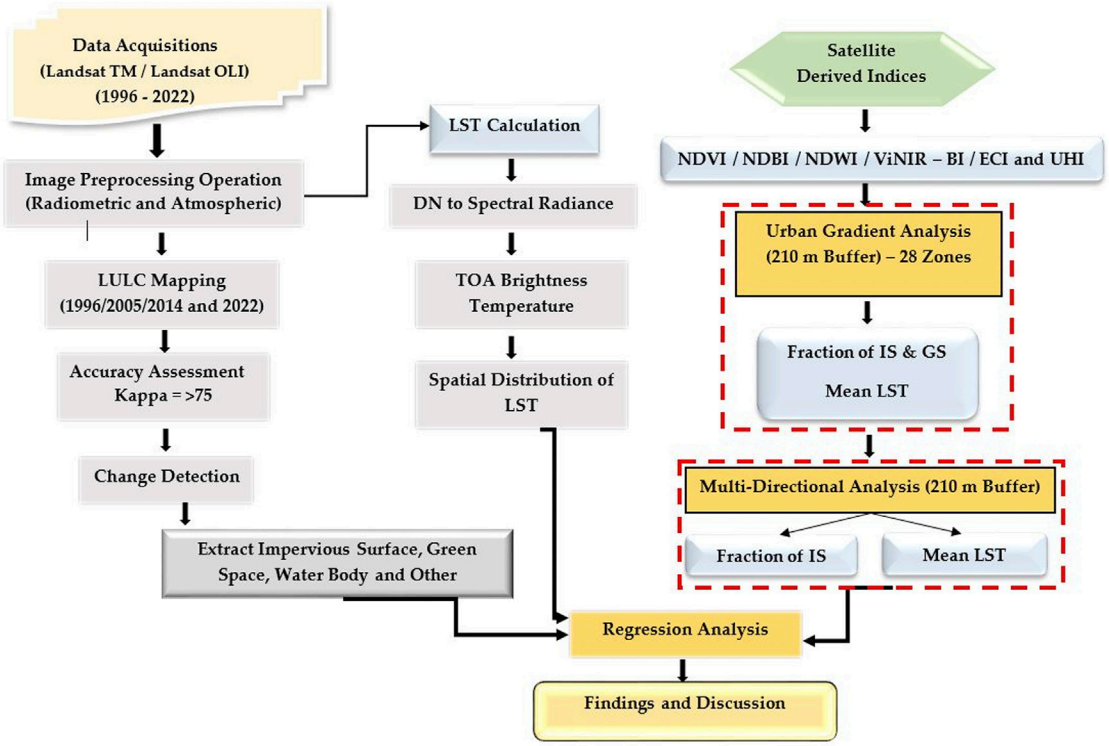

FIGURE 2
Methodological flowchart of the study.

TABLE 2 Details of LU/LC Classes in the study area.

Ref	LU/LC	Details
1	Impervious surface (IS)	Including buildings, roads, and all other impervious surfaces
2	Green surface (GS)	Forest, grassland, and other green areas
3	Water Bodies (WB)	Sea, wetland areas, swamps, irrigation and drainage canals
4	Other (OT)	All other LULC types except to above

2005, 2014, and 2022 using Maximum Likelihood Classification (MLC) algorithm. The same Landsat images were utilized to analyze changes in LST, UHI, IS, GS, and EC. Spatial temporal changes in the landscape were measured through the Maximum Likelihood Classification (MLC) algorithm, along with accuracy assessment. Various remote sensing indices, including UHI, NDVI, NDBI, Normalized Difference Water Index (NDWI), Visible Red and NIR Based Built-up Index (VrNIR-BI), and ECI were calculated to support the detailed analysis. When training data is chosen well, MLC may achieve a high classification accuracy, making it one of the most commonly employed methods for LULC mapping. The spectral characteristics gleaned from training samples are used in supervised image classification. The signature editor was used to manage all of the spectral signatures from the training regions for the images that are being classed (Wijesinghe and Withanage, 2021; Withanage et al., 2024). Also, this is commonly utilized because regional land cover mapping may be achieved at a reasonable cost using medium-resolution satellite remote-sensing data (Weng, 2002; Dissanayake et al., 2019). It depends on how likely a pixel is to belong to a particular class. The LU in the study area was divided into four categories: IS, GS, water bodies, and others (Table 2). Furthermore, Supplementary Figure A1 presents the LULC information in Table 2.

2.3.2 Accuracy assessment

The stratified random sample technique was used to execute the accuracy assessment. To compare the pixels in the identified images with the reference data for each year, these samples were utilized. Independent training points were employed to evaluate accuracy. Throughout the process, 300 points were produced each year that covered all LULC classes (Wu and Murray, 2003). Then, Google Earth was used as reference data in the accuracy assessment. The results were statistically presented using the confusion matrix (Rawat and Kumar, 2015; Mohajane et al., 2018; Liu et al., 2015). It is made up of numbers that are arranged in rows and columns and show the different sample points assigned to each class concerning

the actual ground condition of a particular class (Congalton, 1991). The kappa coefficient provides the intended land-use classification with accuracy.

The user accuracy, producer accuracy, overall accuracy, and lastly, the Kappa coefficient were calculated to measure the accuracy of derived LULC maps (Ziaul and Pal, 2016; Sultana and Satyanarayana, 2018). The degree of agreement between user-given values and predetermined assigned values was determined using the probabilistic Kappa test (Ishtiaque et al., 2017; Bokaie et al., 2019). The following Equations 1–4 are used, in order, to compute the producer accuracy (1), user's accuracy (2), total accuracy (3), and Kappa coefficient (4) (Mirzaei, 2015; United States Geological Survey, 2018).

$$Overall\ Accuracy = \frac{\sum CCP\ (Diagonal)}{\sum CRP} \times 100 \quad (1)$$

where the corrected reference pixels are CRP, and the corrected categorized pixels are CCP (Diagonal);

$$User\ Accuracy = \frac{\sum CCP\ (Category)}{\sum CPC\ (Row)} \times 100 \quad (2)$$

where CCP (Category) is the corrected classified pixels (category) and CPC (Row) is the classified pixels in that category (the row total);

$$Producer\ Accuracy = \frac{\sum CCP\ (Category)}{\sum CPC\ (Column)} \times 100 \quad (3)$$

where CCP (Category) is the corrected classified pixels (diagonals) and CPC (Column) is the classified pixels in that category (the column total);

$$K = \frac{N \sum_{i=j}^{k} x_{ii} - \sum_{i=1}^{k} (x_{i+} \times x_{+i})}{N^2 - \sum_{i=1}^{k} (x_{i+} \times x_{+i})} \quad (4)$$

where k is the number of rows in the matrix; x_{ii} is the number of observations in row i and column i; x_i+ and x + $_i$ (upper and lower right segment of the equation) are the marginal totals of row k and column i. N is the number of observations (Alqurashi and Kumar, 2014).

2.3.3 LST retrieval

LST differences in urban and rural areas can be assessed using various methods, including URGZ analysis and grid-based analysis. These methods have been applied in previous research conducted in urban areas such as Kandy, Kurunegala, and Nuwara Eliya in Sri Lanka (Ranagalage et al., 2018a; Ranagalage et al., 2019; Ranagalage et al., 2020). Landsat Thematic Mapper (TM) data for 1996, and 2005, Landsat 8 Optical Land Imager (OLI), and Thermal Infrared Sensor (TIR) data for 2014 and 2022 were used for the retrieval of LST using the Split-Window (SW) technique. The LST was obtained by Thermal Infrared (TIR) band 6 of Landsat 5 and TIR bands 10 and 11 of Landsat 8 by converting DN values into radiance values (Ranagalage et al., 2017; Sultana and Satyanarayana, 2018; Dissanayake et al., 2019; Jaafar et al., 2020). Here we used thermal bands holding brightness temperatures which are represented in Kelvin. Before LST retrieval land surface emissivity values were derived using below Equation 5 (United States Geological Survey, 2020; Ranagalage et al., 2017; Ranagalage et al., 2018b; Dissanayake et al., 2019).

$$\mathcal{E} = m P_V + n \quad (5)$$

where $\mathcal{E}$ represents land surface emissivity; m represents $(\mathcal{E}_v - \mathcal{E}_s) - (1 - \mathcal{E}_s)\ F\mathcal{E}_v$; P_v represents the amount of vegetation; n represents $\mathcal{E}_s + (1 - \mathcal{E}_s)\ F\mathcal{E}_v$; $\mathcal{E}_s$ is soil emissivity; $\mathcal{E}_v$ is the vegetation emissivity; and F is a shape factor (Ranagalage et al., 2017; Ranagalage et al., 2018a; Dissanayake et al., 2019; Aubard et al., 2019). Here we used $m = 0.004$ and $n = 0.986$ as in previous research (Jaafar et al., 2020; Ranagalage et al., 2017; Dissanayake et al., 2019). The proportion of vegetation (PV) is derived from the Equation 6.

$$PV = \left((NDVI - NDVImin) / (NDVImax - NDVImin) \right)^2 \quad (6)$$

where NDVI is the normalized difference vegetation index derived from Equation 9 as in the section below. The NDVImin and NDVImax are the minimum and maximum values of the NDVI, respectively. Then emissivity corrected LST were retrieved using Equation 7.

$$LST\ (^{\circ}C) = \frac{TB}{1} + (\lambda \times TB/p) In\mathcal{E} \quad (7)$$

where TB = Landsat TM Band 6 at-satellite brightness temperature; λ = wavelength of emitted radiance (λ = 11.5 μm for Landsat TM Band 6, λ = 10.8 μm for Landsat TIRS Band 10); p = h × c/σ (1.438 × 10–2 mK), σ = Boltzmann constant (1.38 × 10–23 J/K), h = Planck's constant (6.626 × 10–34 Js),c = velocity of light (2.998 × 108 m/s), $\mathcal{E}$ is the land surface emissivity. Last, the LST values of Kelvin were converted into degrees Celsius (°C) (Xiao and Weng, 2007; Li et al., 2013; Ranagalage et al., 2017; Dissanayake et al., 2019). After retrieving the LST for each year, the derived maps were reclassified into five classes ranging from low to very high LST using an equal interval method, based on their minimum and maximum values.

The UHI index was employed to describe the UHI phenomenon more intensively in the MC. Typically, high UHI spots indicate the warmer regions within a city. The UHI index was calculated using the Equation 8 as below (Sultana and Satyanarayana, 2020).

$$UHI_{index} = LSTi - LST_{min}\ / LST_{max}\ - LST_{min} \quad (8)$$

LST_i is the LST of grid points in the spatial distribution of LST, $LST_{max,}$ and TST_{min} are the maximum and minimum LST in the study area of the particular year. As proposed by (Xu et al., 2013; Jain et al., 2020) UHI intensity regions were also categorized into five class as very weak UHI, weak UHI, moderate UHI, strong UHI, and very strong UHI.

2.3.4 NDVI calculation

NDVI was used to determine the spatial temporal patterns and quantify the amount of GS in the study area. The GS sustains local climatic variables like precipitation, which is represented by the NDVI (Santos et al., 2017; Estoque et al., 2017). The range of NDVI values is −1 to 1. Negative values in this contrast virtually represent the water bodies (Saputra et al., 2023). On the other hand, the area with thick GS is indicated by an NDVI score close to +1. It is frequently computed using the normalized variance between the near-infrared band and image pixels. Equation 9 was used to derive NDVI (Shikary and Rudra, 2020).

$$NDVI = \frac{NIR_{(Band\,4,5)} - RED_{(Band\,3,4)}}{NIR_{(Band\,4,5)} + RED_{(Band\,3,4)}} \quad (9)$$

The NIR band represents Band 4 in Landsat TM [0.76–0.90 μm (wavelength)] and Band 5 in Landsat OLI [0.85–0.88 μm (wavelength)] respectively, and the RED band represents Band 3 in Landsat TM [0.63–0.69 μm (wavelength)] and Band 4 in Landsat OLI [0.64–0.67 μm (wavelength)], respectively. The GS extraction was performed after masking water bodies and IS in the study area. To extract GS from NDVI maps, a manual threshold technique was used. The thresholds applied were 0.494 for the year 1996, 0.439 for 2005, 0.389 for 2014, and 0.345 for 2022. These thresholds were determined by overlaying the extracted maps onto Google Earth Pro and a color composite of Landsat (Ranagalage et al., 2020).

2.3.5 Deriving NDBI

NDBI is another graphical indicator used to measure IS using satellite data. Positive values in the NDBI values indicate the presence of a built-up area. Typically, the NDBI value falls between −1.0 and +1.0. Vegetation is generally represented by negative values, and IS are shown by positive values. Equation 10, which presents the mid- and near-infrared bands, was used to derive the NDBI (Ranagalage et al., 2018b; Tian et al., 2022).

$$NDBI = \frac{MIR_{(Band\,5,6)} - NIR_{(Band\,4,5)}}{MIR_{(Band\,5,6)} + NIR_{(Band\,4,5)}} \quad (10)$$

the MIR band represents Band 5 in Landsat TM [1.55–1.75 μm (wavelength)] and Band 6 in Landsat OLI [1.57–1.65 μm (wavelength)], respectively, and the NIR band represents Band 4 in Landsat TM [0.76–0.90 μm (wavelength)] and Band 5 in Landsat OLI [0.85–0.88 μm (wavelength)], respectively. The extraction of IS was also conducted using a manual threshold technique, as applied in similar previous research by Ranagalage et al. (2020). The lower threshold values for IS were 0.0471 for the year 1996, 0.102 for 2005, −0.0798 for 2014, and −0.0688 for 2022.

2.3.6 NDWI

NDWI was used to extract water bodies from other LULC classes. Equation 11 was used to derive NDWI in the study area. We also applied Otsu's optimal binary threshold technique to separate the water class from other classes, as described by Ranagalage et al. (2020).

$$\mathrm{NDWI} = \mathrm{Green} - \mathrm{NIR}/\,\mathrm{Green} + \mathrm{NIR} \quad (11)$$

where Green represents band 2 and NIR is band 4 of Landsat 5 images and band 3 (Green) and band 5 (NIR) of Landsat 8 images.

2.3.7 ECI

The ECI was used to identify environmentally critical areas based on the ratio between LST, and NDVI (Weng, 2002; Wu and Murray, 2003). The Built-Up (BU) index, a method based on the differences between the two, was used to determine the difference between the NDBI and NDVI. Urban locations will be easier to distinguish if there are fewer reflections from vegetation. Equation 12 was applied to calculate the BU index (Sapena and Ruiz, 2015; Xiao and Weng, 2007).

$$BU = (NDBI) - (NDVI) \quad (12)$$

The retrieved BU layers were first normalized using the histogram equalization method, which ranges pixel values between 1 and 255. Equation 13 is used to estimate the ECI phenomena (Sapena and Ruiz, 2015; Xiao and Weng, 2007). It has been demonstrated that increases in LST directly correspond with ECI. On the other hand, a claimed negative association exists between declines in GS (Sapena and Ruiz, 2015).

$$ECI = LST \times BU\ (1 - 255\,streched) \quad (13)$$

Then pixel values of derived images are converted into the same ranges between 0 and 1 using the raster normalization technique. The higher the ECI value, the more environmentally critical. Before extraction, the environmentally critical areas of water bodies and green surface were excluded through masking. The spatial variation of ECI over the study area was interpreted as very high (0.75–1), high (0.5–0.75), moderate (0.3–0.5), low (0.25–0.3), and very low (<0.25) as similar to the previous study conducted by (Ranagalage et al., 2017).

2.3.8 Urban-rural gradient and UHI profile analysis

The urban-rural gradient zone analysis was used to examine the relationship between LST, the Fraction of IS (FIS), and the Fraction of GS (FGS) with changing distance from the city center. This method has been applied in many previous studies on single-core cities to identify the spatial variations of LST, IS, and GS (Estoque and Murayama, 2017; Estoque et al., 2017; Ranagalage et al., 2019; Ranagalage et al., 2020). The URGZs were derived following several steps. First, 210 m × 210 m fishnet grids were prepared by snapping the derived LST, NDBI, and NDVI maps. Second, twenty-eight URGZs were created, considering the maximum distance from the city center to the MC boundary (5.8 km). Here, the Galle city center was considered as the 0 grid. Third, the mean LST, fraction of IS, and fraction of GS were calculated for each zone using the zonal statistics tool. Finally, regression analysis and scatter diagrams were used for further analysis (Ranagalage et al., 2019; Ranagalage et al., 2020). Multi-directional and multi-temporal variations of the UHI profile were analyzed by examining the relationship between mean LST, FIS, and FGS along orthogonal and diagonal directions from the city center. Since Galle city is bounded by the ocean on three sides, it was possible to derive three directional analyses: north-south, northeast-southwest, and northwest-southeast.

2.3.9 Grid analysis

This method is also widely used in previous research on LST and landscape structure analysis (Myint et al., 2010; Estoque and Murayama, 2017; Ranagalage et al., 2019; Ranagalage et al., 2020). To analyze the spatial relationship among mean LST, FIS, and FGS, a 210 m × 210 m (7 × 7 pixels) grid was used, as previous studies in the same domain have proven this grid size to produce better correlations.

2.3.10 Landscape expansion index (LEI)

Nonetheless, utilizing multi-temporal remote sensing data, the widely used LEI has shown promise in capturing the evolution of impervious surface patterns (Tian et al., 2022). There are three types of urban landscape extension patterns: outlying, edge, and infilling.

"Edge-expansion" denotes the type that extends beyond the edge of the urban built-up area; "outlying" denotes the type of newly grown urban patches that are separated from the built-up area; and "infilling" denotes the type where undeveloped patches in built-up urban areas are filled with newly grown impervious surface patches (Tian et al., 2022). The LEI, which is computed for new IS areas using Equation 14, offers a more profound understanding of IS and temporal dynamics (Sapena and Ruiz, 2015).

$$LEI = \frac{l_c}{p} \times 100 \tag{14}$$

where, l_c = length of the shared edge and p = perimeter of the new object. It ranges from 0 to 100, where the infilling type is $100 \geq > 50$ (expansion is occurring within or adjacent to already developed areas), edge-expansion $50 \geq > 0$ (urban growth is extending outward along the periphery of current urban areas rather than creating new isolated patches or filling in gaps within the urban core), and outlying = 0 (new development is occurring as isolated patches separate from the established urban area, rather than expanding along the edges or filling in existing gaps) (Sapena and Ruiz, 2015).

2.3.11 Statistical analysis

To analyze the relationship between LST and other remote sensing indices, simple Ordinary Least Squares (OLS) regression analysis was performed using MS Excel. The level of coefficients in all linear regression results was reported as statistically significant ($p < 0.001$). Based on these regression results, scatter plots between LST, FIS, FGS, and other remote sensing indices were created for the years 1996, 2005, 2014, and 2022. LST, NDVI, and NDBI, NDWI, FIS, FGS pixel values were transformed into points for this purpose. Additionally, triangle heat map based on Origin Pro were prepared for each year to cross-check the relationship between LST and other indices.

3 Results

3.1 Structural changes of the landscape

Among the four LULC classes, the findings indicate that impervious surface has shown the most significant expansion over the past 26 years. Throughout the study period, impervious surface areas grew mostly gradually, from 5.5 km^2 (31.7%) in 1996 to 12.8 km^2 (74.1%) in 2022 with indicating a 7.3 km^2 growth. This rapid growth of impervious surface occurred at the continuous expense of green surface, which decreased from 5.6 km^2 to 1.7 km^2 (−3.9 km^2) during the concerned period. In addition to green surface, 3.4 km^2 areas including paddy lands and homesteads categorized under "other" have also been converted into other LULC over the last 26 years. Considerable changes in the water bodies, could not be detected since the MC area consists only of a few canals and marshes. The overall accuracy rates exceeded the recommended minimum standard of 75%, indicating a reliable classification of LULC for each year. The Kappa coefficient was 0.84 in 1996, 0.82 in 2005, 0.80 in 2014, and 0.78 in 2022 as Supplementary Table A1. The classified LULC maps in the Galle MC area for 1996, 2005, 2014, and 2022 are visualized in Figure 3 and quantified in Table 3.

Impervious surface comprised 5.5 km^2 of the total land area in 1996 and by 2014 it has gradually increased up to 9.7 km^2. However, by 2022, it can be seen how new impervious surface have been created in areas with green surface and other LU types as expanding impervious surface into 12.8 km^2. The LULC transition during the study period is visualized in Supplementary Figures A2, A3. Based on those figures and statistics, approximately 3.5 km^2 of green surface and 3.8 km^2 of other land use types were converted into impervious surface over the last 26 years. The rapid expansion can be detected in the central and southern areas of MC that are near to city core. These spatial-temporal variations in the LULC classes impacted the ecosystem health and LST and UHI intensity during the study period.

3.2 Variations of LST and UHI intensity distribution

Figure 4 depicts the spatial distribution of LST in the Galle MC area for the years 1996, 2005, 2014, and 2022. In 1996, high LSTs were concentrated in the city core. LST varied from 21.06°C to 32.4 C in 1996, with a mean of 26.4 C. However, by 2005, areas with high LST had substantially grown towards the eastern and central parts and along the coastline, following the expansion pattern of impervious surface. During this period, the mean LST has increased to 28.9°C, showing an increase of 2.5 C. This trend continued until 2022, with the maximum LST increasing from 33.2°C to 33.7 C and the mean temperature rising from 28.9°C to 29.1 C between 2005 and 2022, although the minimum LST fluctuated slightly around 2014 as shown in Supplementary Table A2. High LST began to extend in and around the city center area in 2014. In 2022, the city core and its surrounding areas had higher LST values, which were dispersed mostly to the northern and eastern parts of MC. The link between LST and the pattern of impervious surface expansion is well demonstrated along road networks and growth nodes. LST increased in the core areas, while the southern beach area experienced significant LST changes due to impervious surface expansion and a loss of green surface. Throughout the entire period, most green surface in the northeastern and northwestern regions have maintained comparatively low LST.

Results further revealed that the UHI intensity in the MC area has also increased significantly over the 26 years as shown in Figure 5. The data on UHI intensity over the years indicates a substantial increase in both the minimum and maximum UHI intensity values, reflecting a growing severity of the UHI effect. In 1996 the UHI intensity ranged from a minimum of −2 C to a maximum of 1°C. This suggests that surrounding areas of the Impervious Surface core were cooler than the city areas (negative UHI intensity), while other areas experienced only a slight UHI effect. The UHI intensity increased significantly by 2005, with a minimum of 4.5 C and a maximum of 9 C. This indicates that most areas within the city were warmer than their rural counterparts, with a marked increase in the intensity of the UHI effect compared to 1996. In 2014 minimum UHI intensity further increased to 6°C, while the maximum remained at 9 C.

This demonstrates a continuing trend where the entire impervious surface is experiencing higher temperatures relative to rural areas, with the minimum intensity rising closer to the

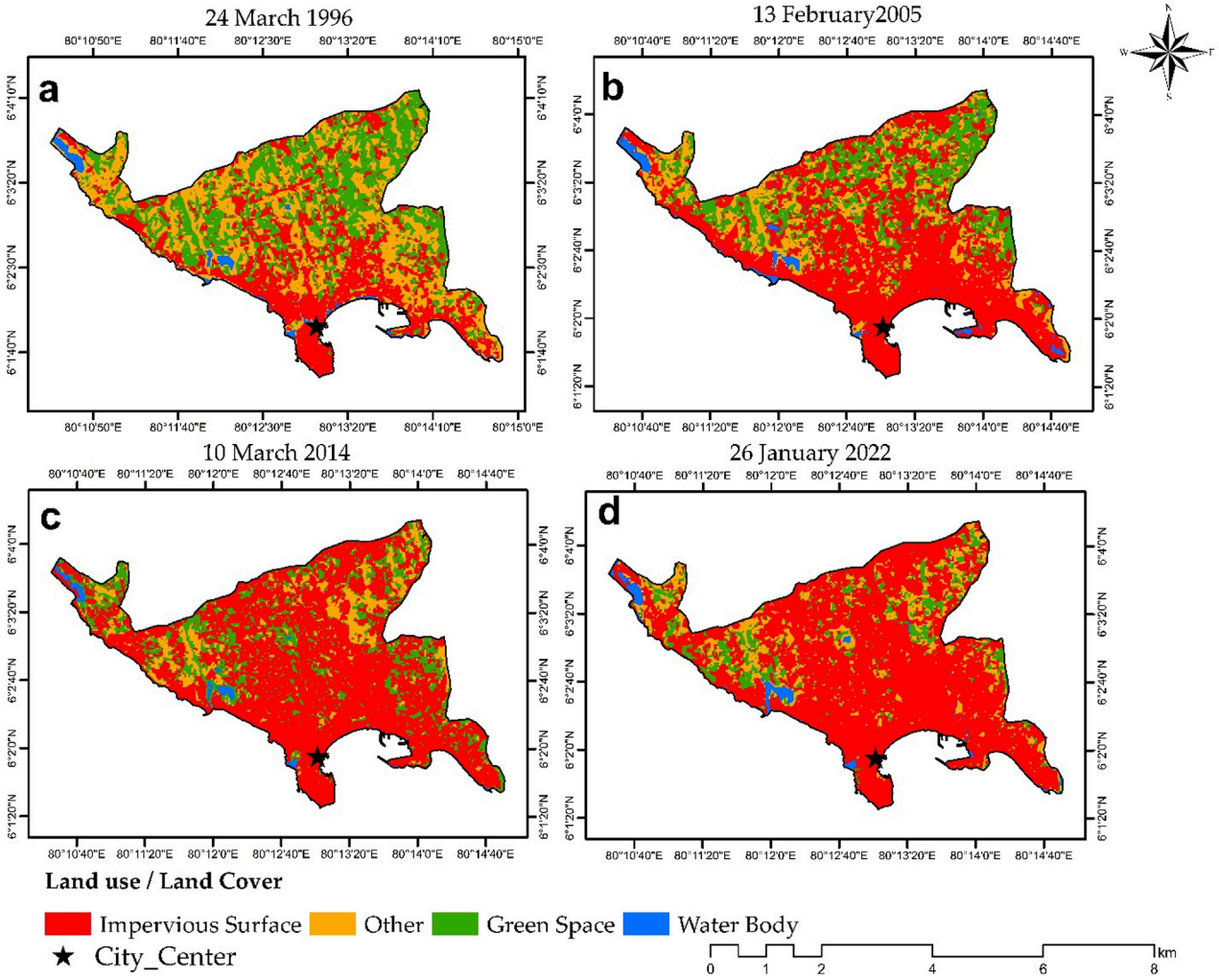

FIGURE 3
Classified LULC maps for the Galle MC **(A)** 1996, **(B)** 2005, **(C)** 2014, and **(D)** 2022.

TABLE 3 *LULC changes in Galle MC (1996–2022).*

Land cover									Land cover changes			
LULC	1996	%	2005	%	2014	%	2022	%	1996–2005	2005–2014	2014–2022	1996–2022
IS	5.50	31.76	9.79	56.51	11.93	68.90	12.84	74.15	+4.2	+1.3	+0.91	+7.34
GS	5.67	32.71	3.76	21.70	3.25	18.74	1.76	10.19	−1.9	−0.5	−1.4	−3.9
WB	0.44	2.54	0.43	2.45	0.25	1.43	0.43	2.47	−0.01	−0.18	+0.18	−0.01
OT	5.71	32.98	3.35	19.34	1.89	10.93	2.28	13.19	−2.4	−1.5	+0.4	−3.4
Total	**17.32**	**100**	**17.32**	**100**	**17.32**	**100**	**17.32**[a]	**100**[b]	-	-	-	-

[a]Is the total area in km^2.
[b]Is the total area in percentage.

maximum intensity of the previous period. The minimum UHI intensity reached 7 C by 2022, and the maximum increased to 10.5 C. This data suggests that the UHI effect has become even more pronounced, with both the minimum and maximum intensities showing significant increases. The impervious surface is now consistently experiencing higher temperatures, and the peak intensity of the UHI effect has reached new highs. Overall, this progression indicates a consistent and substantial increase in UHI intensity over the 26 years, highlighting the growing impact of impervious surface and the associated changes in LULC on local

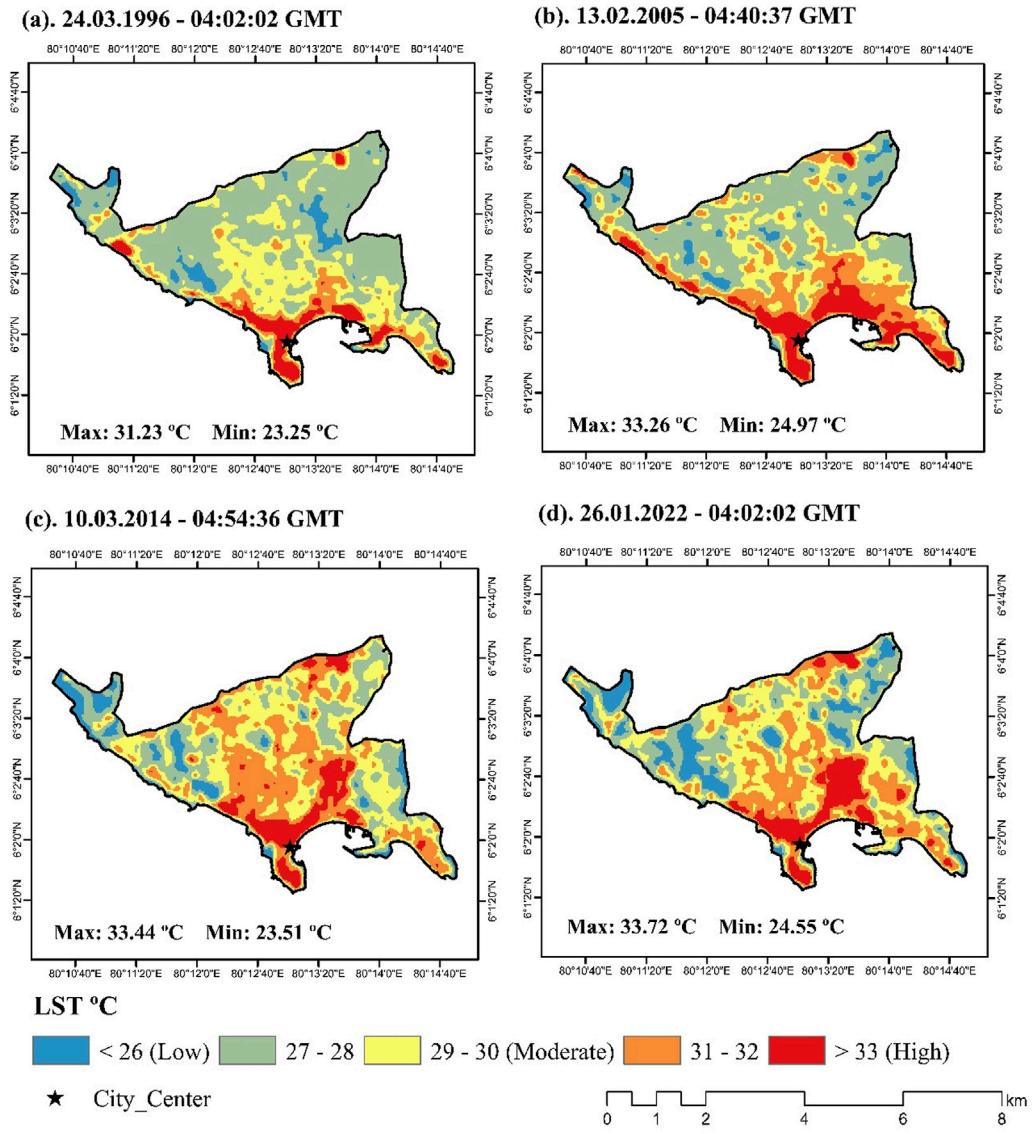

FIGURE 4
Spatial variations of LST in Galle MC; **(A)** 1996, **(B)** 2005, **(C)** 2014, **(D)** 2022.

climate conditions. Figure 6A [1, 2, 3, 4], (c) [8, 9, 10] further demonstrates that the majority of weak UHI areas and low LST areas consist of existing green surfaces from 1996 to 2022. Additionally, areas with high LST and changes in the HUI correspond to high-density impervious surface development during this period, as shown in Figure 6B [5, 6, 7], (d) [11, 12, 13]. Flooring, roofing, and concrete structures have disrupted the surface energy balance by reducing evapotranspiration and increasing sensible heat in the city core. This is the main reason for the day and night UHI intensity anomalies between impervious surface and other LULC types.

3.3 Relationship between LST and other biophysical indices

Supplementary Figure A4 illustrates the derived NDVI maps during four distinct periods, namely, 1996, 2005, 2014, and 2022. Supplementary Table A3 also summarizes descriptive statistics. The minimum NDVI values have increased from −0.53 in 1996 to −0.11 in 2022. This suggests a reduction in the number of areas with very low or negative vegetation indices. The maximum NDVI values have slightly decreased from 0.71 in 1996 to 0.51 in 2022. This indicates that the areas with the highest green surface or healthiest green surface have seen a decline, suggesting potential degradation of the most vegetated areas. The mean NDVI values have decreased from 0.41 in 1996 to 0.26 in 2022. This overall decline in the mean NDVI indicates a general reduction in environmental health and green surface over the years. The results suggest that over the period from 1996 to 2022, there has been a noticeable decrease in vegetation health and green surface density. Overall, mean and maximum NDVI values have declined, pointing to a general degradation in green surface quality and coverage as a result of the expansion of impervious surface.

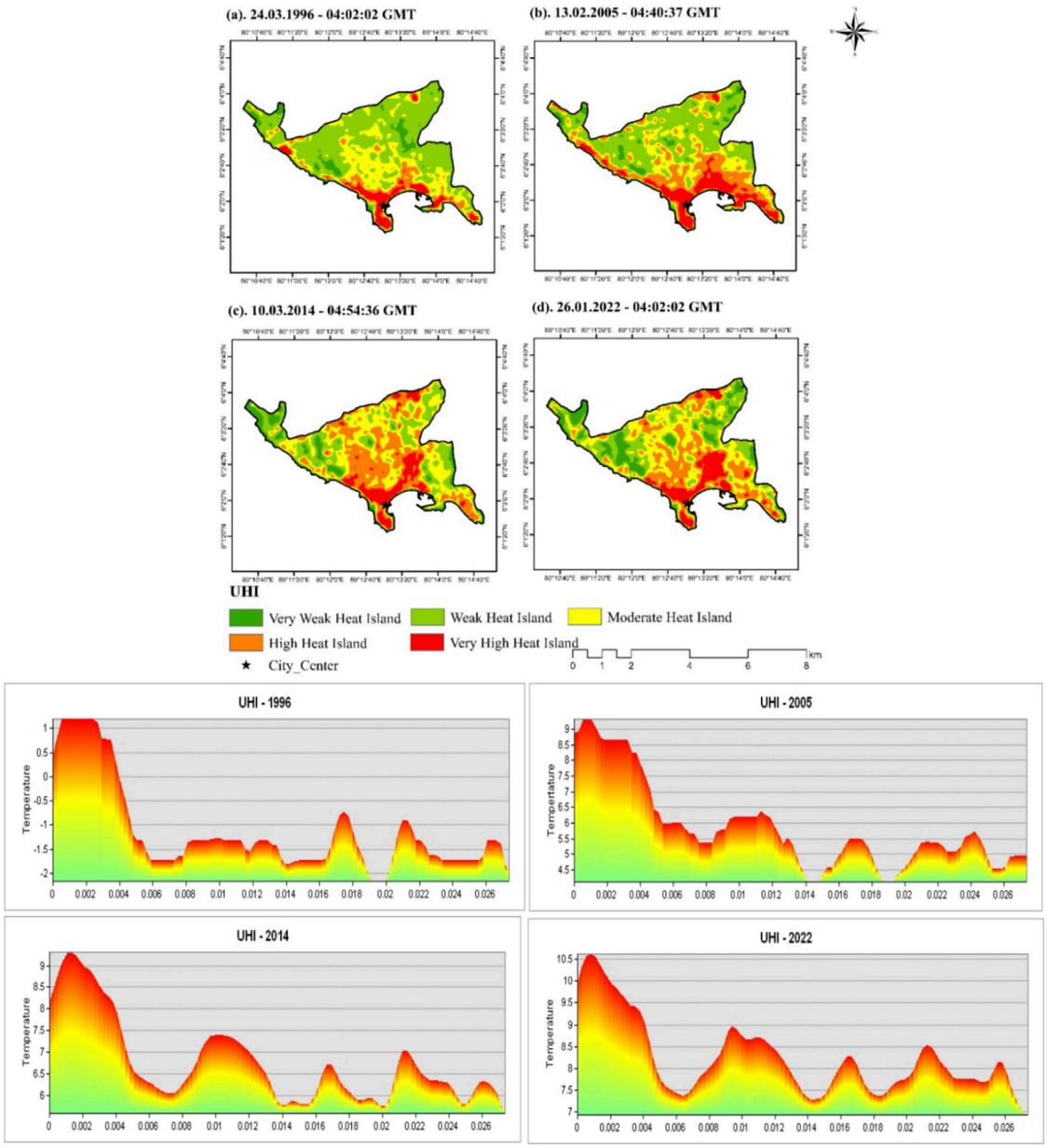

FIGURE 5
UHI intensity in Galle MC: **(A)** 1996, **(B)** 2005, **(C)** 2014, **(D)** 2022; Distribution of UHI intensity profile from city to MC boundary.

The minimum NDBI values (Supplementary Figure A4; Supplementary Table A4) have increased from −0.57 in 1996 to −0.37 in 2022. This suggests that the areas with the lowest NDBI values. The maximum NDBI values have decreased slightly from 0.46 in 1996 to 0.19 in 2022. The NDBI data indicates that from 1996 to 2022, there has been a complex pattern of changes in impervious surface. The minimum NDWI values have increased from −0.62 in 1996 to −0.49 in 2022 (Supplementary Table A5). This suggests that the driest areas have become slightly less dry over time, potentially indicating a decrease in extreme water scarcity in certain areas. The maximum NDWI values have decreased from 0.58 in 1996 to 0.21 in 2022. This indicates that the areas with the highest water content or surface water presence have seen a significant reduction, suggesting a decrease in the extent or presence of surface water bodies.

Regression results derived R^2 0.1962 between LST and NDVI for year 1996 as shown in Supplementary Figure A5. This suggests a weak positive relationship, indicating that only about 19.62% of the variation in LST can be accounted for by the NDVI. But, in 2005 the relationship is stronger with R^2 0.3241 compared to 1996, with about 32.41% of the variation in LST being explained by NDVI. This suggests a moderate positive correlation. By 2014 The relationship is quite weak with R^2 0.1084, with only 10.84% of the variation in LST explained by NDVI, indicating a low positive correlation. In the year 2022 with R^2 0.2571 there is a moderate relationship, with 25.71% of the variation in LST being explained by NDVI, which is stronger than in 2014 but weaker than in 2005. Overall, these R^2 values suggest that the relationship between LST and NDVI varies over time, being strongest in 2005 and weakest in

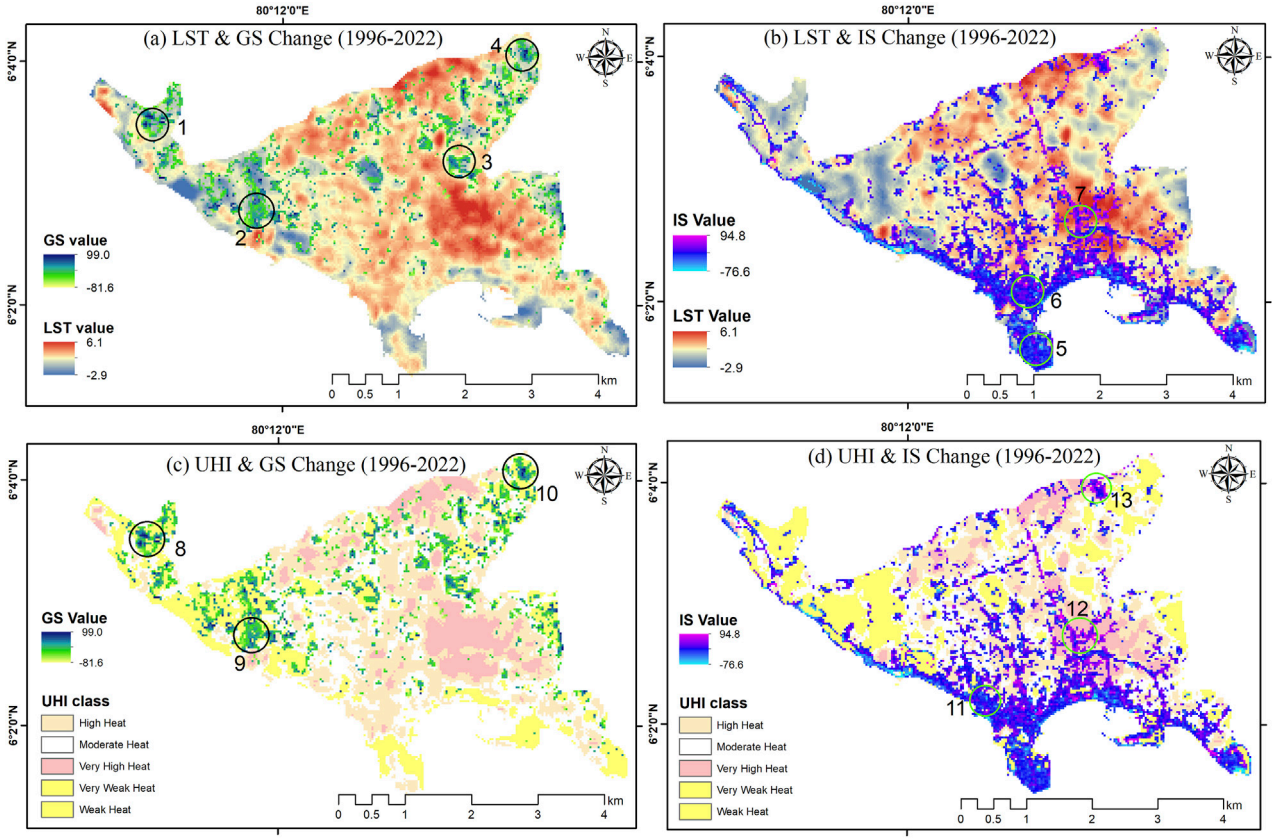

FIGURE 6
GS, IS, LST,UHI change during 1996–2022 **(A)** LST and GS change, **(B)** LST and IS change, **(C)** UHI and GS change, **(D)** UHI and IS change.

2014. The values indicate that NDVI can partially explain changes in LST.

The regression results derived R^2 0.4570 between LST and NDBI for the year 1996. This indicates a moderate positive relationship between LST and NDBI. About 45.70% of the variation in LST can be explained by NDBI. In 2005 also the relationship remains moderately strong, with 45.20% of the variation in LST being explained by NDBI with R^2 0.4520. This is very similar to the relationship in 1996. In year 2014 with R^2 0.3519 the relationship is weaker compared to 1996 and 2005, indicating a moderate but decreased positive correlation. In year 2022, the relationship is moderately strong, with R^2 0.4639 of the variation in LST being explained by NDBI, slightly stronger than in previous years. Overall, these R^2 values suggest that the relationship between LST and NDBI is consistently moderate, with NDBI explaining a substantial portion of the variation in LST. The values indicate that impervious surface, as measured by NDBI, have a significant and relatively stable influence on LST over the years, with the strongest relationship observed in 2022.

Overall, the R^2 values suggest that the relationship between LST and NDWI is generally weak, with NDWI explaining only a small portion of the variation in LST. The strongest relationship was observed in 2005 (R^2 0.2589), indicating that water presence, as measured by NDWI, had a more substantial influence on LST in that year compared to other years. The regression results revealed that R^2 values indicate the relationship between NDVI and NDBI has strengthened over time, with the correlation becoming very strong by 2022 with R^2 0.7519. This trend suggests that as impervious surface areas have increased, green surface has correspondingly decreased, reflecting the significant impact of urban expansion on green surface. The correlation matrix between LST with NDVI, NDBI, NDWI over the four-time period are graphically represented in Figure 7 below.

3.4 LST distribution along URGZs

Derived 28 URGZ, showing the distribution of impervious surface and green surface in the Galle MC area within a 210-meter radius from the city center (Figure 8). This URGZ distribution map clearly illustrates that FIS decreases as one moves away from the city core, while FGS increases with distance from the city center. The map shows that impervious surface density decreased from the urban core toward the rural periphery from 1996 to 2022, while green surface density increased, particularly from 2005 onwards. Figure 9 shows the spatial pattern of mean LST and the FIS and FGS along 28 URGZs. The highest mean LST value was recorded in URZ_1 near the city center. The highest mean LST, ranging from 28.3°C to 27.1°C, was concentrated within URGZs 1 to 7. In 1996, the lowest mean LST was recorded in URGZs 24, 25, and 26, with temperatures of 25.4°C, 25.5°C, and 25.6°C. The mean LST in $URGZ_1$ was 28.3°C in 1996 and increased to 31.7°C, 30.3°C, and 30.7°C by 2005, 2014, and 2022, respectively. Additionally, the mean LST of all other URGZs increased

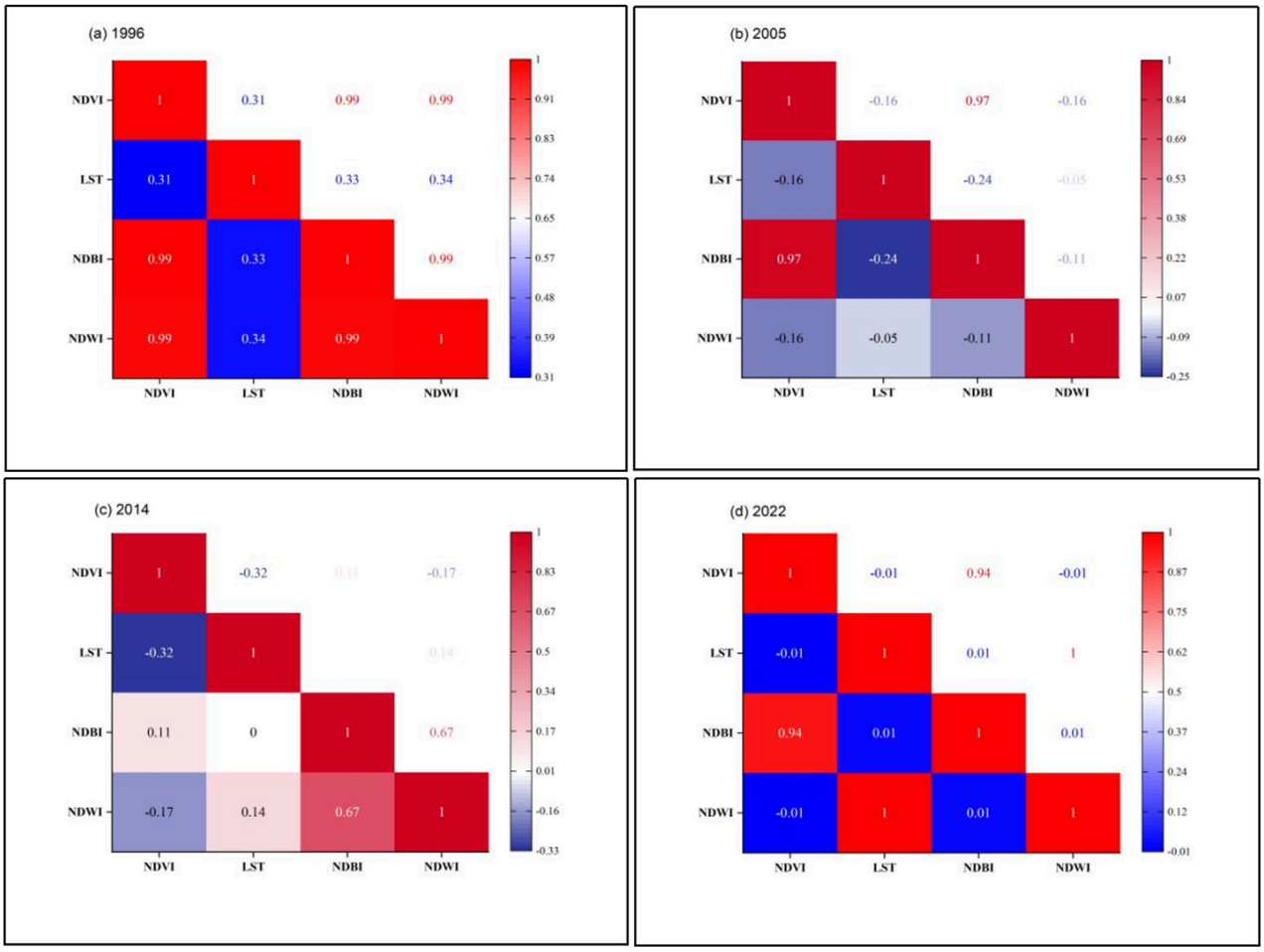

FIGURE 7
The correlation matrix between LST with NDVI, NDBI, NDWI **(A)** 1996; **(B)** 2005; **(C)** 2014; **(D)** 2022.

from 1996 to 2022. The lowest mean LST in 2005 was reported in $URGZ_{25}$ at 27.7°C. In 2014, the lowest mean LST was reported in $URGZ_{26}$ at 26.1°C. In 2022, the lowest mean LST was concentrated in $URGZ_{24}$ at 27.3°C.

The FIS within all URGZs has been rapidly increasing from 1996 to 2022. The highest FIS reported in 1996 years was 10.2% in $URGZ_3$. In 2005, the highest FIS was reported in $URGZ_9$ at 8.2%. In 2014, the highest FIS was reported in $URGZ_8$, as at 7.8%. By 2022, $URGZ_9$ reported the highest FIS at 7.5%. The lowest FIS in 1996 was located in $URGZ_{21}$ at 0.2%. In 2005, the lowest FIS (0.27%) was reported in $URGZ_{23}$. In 2014, the lowest FIS was located in $URGZ_{24}$ at 0.33%. In 2022, the lowest FIS was reported in $URGZ_{26}$ at 0.36%. In 1996, the highest FGS was located in $URGZ_{12}$ at.

11.2%. By 2005, $URGZ_{13}$ reported the highest FGS at 13.4%. In 2014, the highest FGS was located in $URGZ_{15}$, recorded at 13.5%. By 2022, the highest FGS was reported in $URGZ_{14}$ at 11.9%. The lowest FGS in 1996 and 2022 was recorded in $URGZ_{28,27}$, respectively. In 2022, the FGS was reported at 0.05% for $URGZ_{28}$ and 0.06% for $URGZ_{27}$. Overall, the R^2 values show that while there is a strong relationship between mean LST and the fraction of impervious surfaces along $URGZ_{1\text{-}28}$, this relationship has weakened little, particularly in the year 2022 (R^2 0.2631). Conversely, the mean LST showed a moderate negative relationship with the FGS across three time periods except in 2014.

3.5 Multi-directional LST profile

Figure 10 shows multi-directional and multi-temporal profiles of the mean LST and FIS for the years 1996, 2005, 2014, and 2022. The mean LST shows a decreasing pattern from the city center to $URGZ_{17}$ in the north-south direction for all years from around 32°C–26°C. But, for the northeast-southwest and northwest-southeast directions from the city center, the mean LST shows a decreasing trend with some fluctuations. In all three directions and across temporal dimensions, FIS is showing a rapidly increasing trend, particularly noticeable in $URGZ_{1\text{-}4}$.

3.6 Association of mean LST, FIS, and FGS within grid

The spatial distribution and concentration patterns of mean LST, FIS (%), and FGS (%) in the urban core across the 210 × 210 m

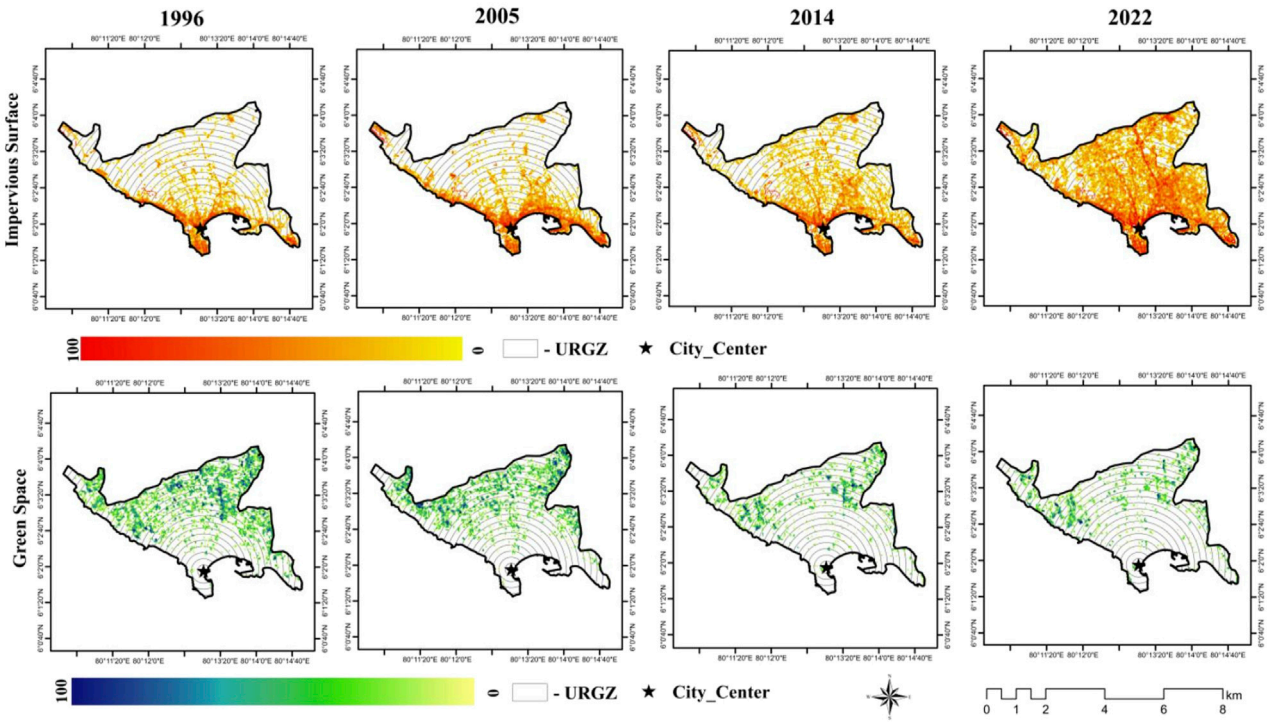

FIGURE 8
The distribution pattern of impervious surface, green surface along URGZs Galle MC.

grid zone from 1996 to 2022 are shown in Figure 11. The results showed that the highest mean LST, exceeding 33°C, was concentrated on the left side of the city core in both 1996 and 2005. However, in 2014 and 2022, the pattern changed to concentration and no longer showed dispersion. Additionally, in 2014 and 2022, the LST within the urban core (210 m × 210 m) grid areas showed a considerable decrease compared to the situation in 1996 and 2005. The beachside consistently exhibited lower mean LST, ranging from 26°C to 30°C, during all four time points. During all four time points, a high fraction of IS was distributed along the northern side of the city core. Comparatively low FIS was observed in the southwestern part of the urban core until 2014. After 2014, a few vegetation patches occupied that area. Due to Galle City inherently evolving as a fortress city and being a UNESCO World Heritage site, the urban core area, extending 210 m × 210 m, is primarily occupied by the fort and other historical buildings, rather than new constructions and green surface. Statistical analysis revealed a low positive but increasing trend in the relationship between mean LST and FIS within Galle MC, with an R^2 value of 0.0784 in 1996 and 0.2919 in 2022 (Supplementary Figure A6). Overall, the relationship between mean LST and the fraction of green surface showed fluctuations, with the strongest correlation occurring in 2014 (R^2 0.1927).

3.7 Landscape expansion patterns in galle MC

The growth patterns of the urban landscape of the Galle MC were derived for three distinct periods: 1996–2005; 2005–2014; 2014–2022 (Supplementary Figure A7; Supplementary Table A6). The expansion of Galle City is mostly compacted, making the IS more continuous, as illustrated in fragmentation metrics, when one considers the compact growth as a mix of infilling and edge–expansion. It is also a unique feature that no outlying patches can be identified in the IS within all three-time period. The LEI pattern was determined based on edge expansion and infilling. The % of edge-expansion patches were 99.9%, 95.46%, and 99.46% in the three periods, indicating a rising tendency. An overview of the three periods reveals that edge expansion is higher than infilling. The proportion of infilling patches was 0.0054%, 4.53%, and 0.55% during the 3 decades. From 2005 to 2014, there was notable growth, and from 2014 to 2022, there was an overall pattern of first increasing and then decreasing. Throughout all periods, the quantity and size of edge-expansion patches were continuously greater than those of infilling patches.

3.8 Environmental criticality in galle MC

Environmental criticality maps for the Galle MC area, derived by combining LST and NDVI images in the Galle MC area following the steps described in the methodology section, are illustrated in Figure 12. When deriving the ECI maps, all areas covering green surface and water bodies were excluded, as these areas have no criticality. According to the derived maps, the EC has increased from 1996 to 2022, with very high and high critical areas concentrated and expanding outward from the city core. In the year low EC areas were

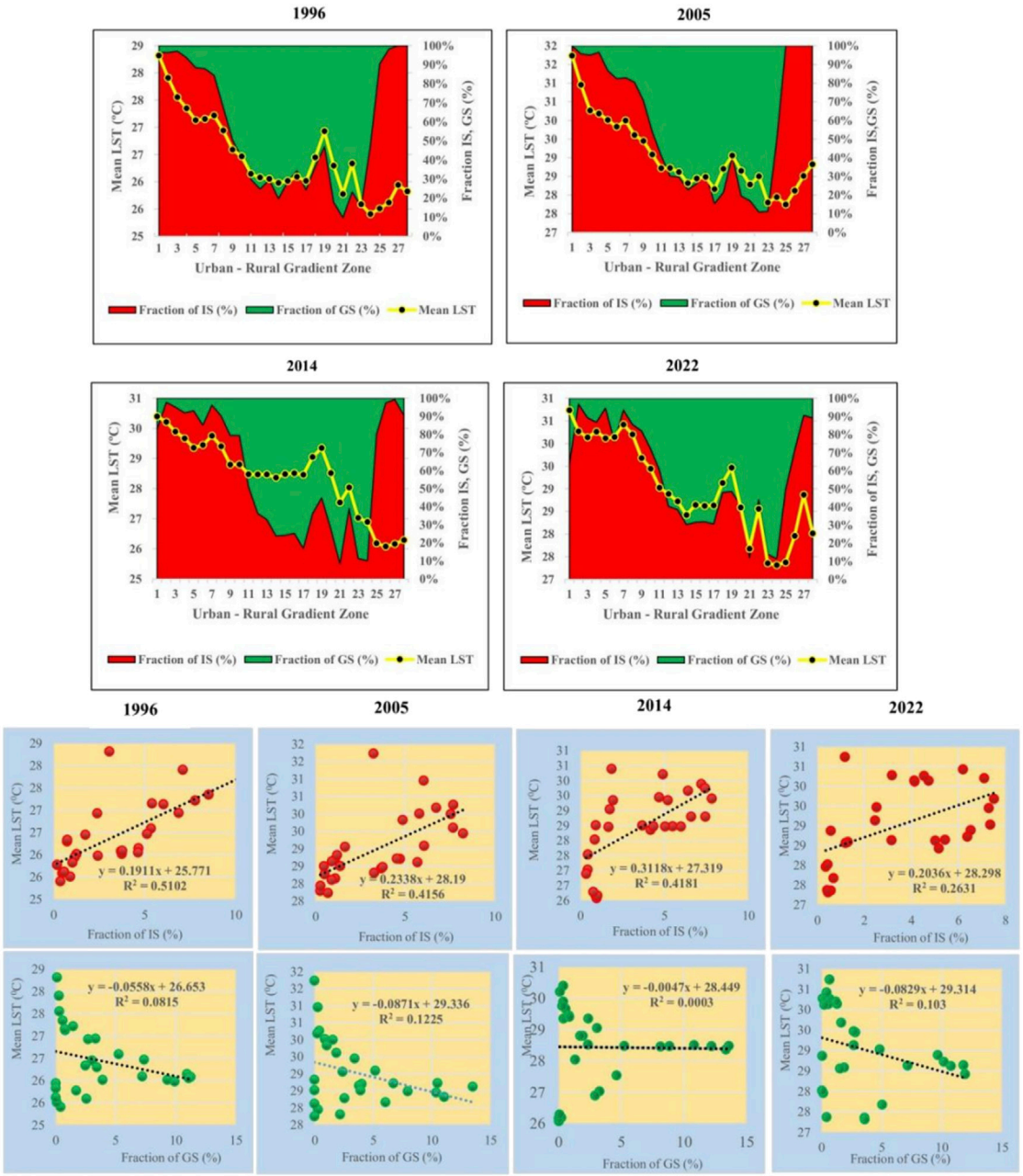

FIGURE 9
The distribution pattern of mean LST,FIS, FGS along URGZs; Results of linear regression between mean LST,FIS and FGS along URGZ, 1996, 2005, 2014 and 2022.

reported in $URGZ_{24}$ as 0.27% while zone 8 reported high EC areas as 7.35%. In the year 2005 low EC area coverage was occupied in $GRGZ_{23}$ at 0.33% and high EC area coverage was reported by zone 9 (8.44%). In 2014 low spatial coverage of EC was occupied in $URGZ_{24}$ (0.30%) while high coverage could be seen in zone 10 (7.76%). Overall, low or very low EC areas could be observed on the northwestern and northeastern periphery of MC in all four time points. The ECI typically follows the distribution pattern of LST (Figure 4) and NDBI values (Supplementary Figure A4) in the study area.

4 Discussion

4.1 Effect of landscape changes on LST and UHI intensity

The results found that the growth of the impervious surface came at the cost of reduced green surface from 1996 to 2022. The extent of green surface decreased from 5.6 km² (32.7%) in 1996 to 1.7 km² (10.9%) in 2022. A 3.57 km² area covered by green surface and a 3.8 km² area under another category was solely transformed

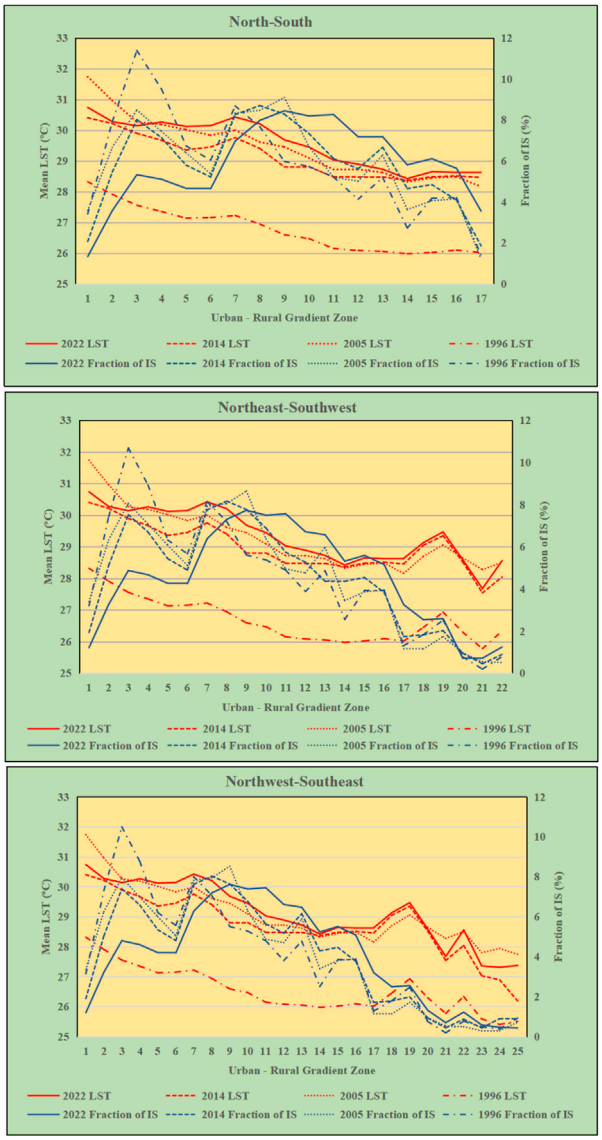

FIGURE 10
Multi-directional UHI profiles in Galle MC based on the mean LST and the FIS.

into impervious surface within the concerned period. This trend is comparable to the previous research findings observed in the Galle MC (Dissanayake, 2020) as well as other cities like Colombo (Fonseka et al., 2019; Senanayake et al., 2013; Ranagalage et al., 2017), Kandy (Ranagalage et al., 2018a), Kurunegala (Ranagalage et al., 2020), and Nuwara Eliya (Ranagalage et al., 2019). Similar landscape changing patterns were also observed by Dissanayake (2020) which demonstrated the rapid transformation of green surface and other areas into impervious surface during the last 2 decades (Dissanayake, 2020). The findings indicated that there was minimal or no significant alteration in water bodies. The increase in residential, administration, and commercial establishments leads to the absorption of most green surface and other LULC types by the impervious surface. The urban growth in the Galle MC was driven by the swift transformation of green surface into impervious surface between 1996 and 2022. This has resulted in the emergence of detrimental consequences, such as the formation of urban heat islands with increasing EC.

The results of this study provided evidence of increasing LST and UHI intensity. The mean LST in the Galle MC has experienced a 2.7 C increase between 1996–2022, as shown in Figure 4. Also, the UHI intensity index has shown a considerable increase from 1°C to 10°C during the concerned period (Figure 5). The URGZ analysis results also demonstrated that UHI intensity is concentrated within a 1.5 km^2 radius from the city core. The spatial and temporal distribution patterns of mean LST and FIS provide a clear image of the relationship between UHI intensity expansion and impervious surface expansion between 1996 and 2022. On the other hand, the mean NDVI has decreased by 0.15 within 26 years. Especially, afterward 2005 increasing LST zones has expanded parallel to the impervious surface expansion direction. The cause of this phenomenon might be attributed to the recently developed urban areas, as indicated by Dissanayake (2020). Urban expansion in the Galle MC may lead to a subsequent rise in the overall LST and UHI intensity shortly. The declining NDVI and inclining NDBI have further supported this trending pattern. Though, LST and NDVI have low negative relationship and values indicate that NDVI can partially explain changes in LST, the inverse correlation between LST and NDBI indicates that impervious surface have a direct effect on raising the overall LST and UHI intensity in the study area. The distribution maps of NDBI and ECI also indicate that impervious surface areas with higher LST are more susceptible to environmental criticality. Newly added impervious surfaces in the study area may lead to an increase in the vulnerability of LST (Dissanayake, 2020) and ECI.

4.2 Trends of urban growth in MC

The findings indicated that the Galle MC underwent considerable landscape transformations during 1996–2022, as demonstrated by the rapid expansion of impervious surface. Throughout the 26 years, the impervious surface expanded by 7.34 km^2 (Table 3). The rapid expansion of impervious surface occurred more during 1996–2005. Dissanayake (2020) also found that the Galle MC displayed a comparable trend of urban expansion, which aligns with the findings presented in this study (Dissanayake et al., 2019). The URGZ analysis results also proved that FIS decreases as one moves away from the city core, while FGS increases with distance from the city center. High fraction of impervious surface could be observed within URGZ$_{1\text{-}9}$ and it gradually decreased toward rural periphery while green surface density increasing. However, that study discovered that the increase of the built-up area primarily occurred in a north-south direction. The expansion trajectory of Galle City exhibits similarities to other growing cities like Kandy and Kurunegala, where evidence of the UHI effect has been documented (Fonseka et al., 2019; Senanayake et al., 2013; Ranagalage et al., 2017; Ranagalage et al., 2019; Dissanayake et al., 2019; Ranagalage et al., 2020). Though, Ranagalage et al. (2020) discovered that urban expansion in Kurunegala primarily took place in the southern direction, following a linear pattern, in Galle, it is apparent that urbanization occurred mainly along the north-south direction showing a compacted growth as Figure 10 (Ziaul and Pal, 2016). This growth pattern is related to the location of MC as a coastal city,

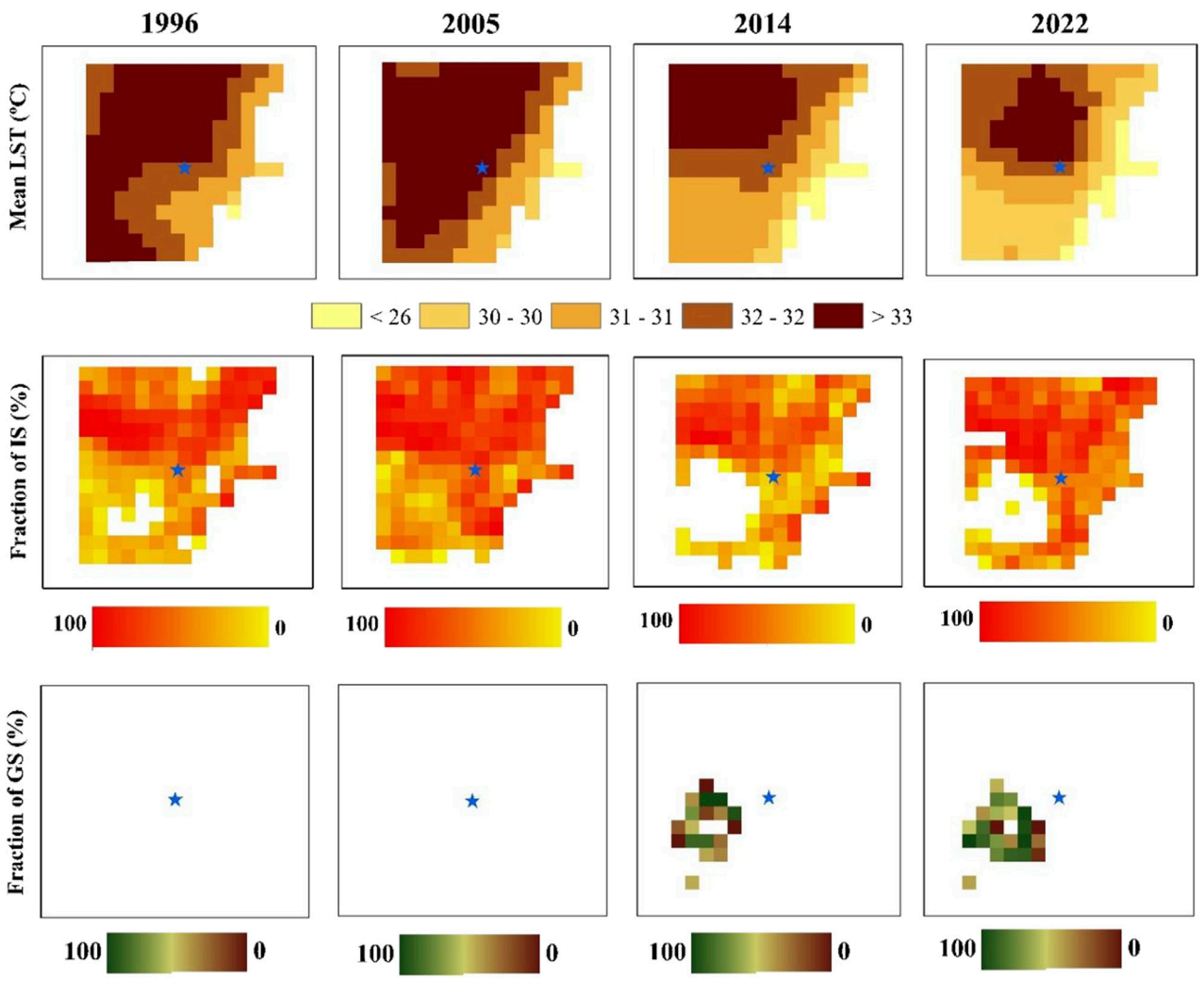

FIGURE 11
210 × 210 m polygon grid showing maps of the Mean LST, FIS (%), and the FGS (%) in 1996, 2005, 2014, and 2022 in Galle urban core.

which limits its expansion towards the south which collaborated with the findings of Dissanayake (2020). However, due to the rich urban heritage dating back to the colonial era, the city is linked to other cities such as Matara and Kalutara via the A2 road. Indeed, the urban expansion along the A2 road is also significant. The improved physical and social infrastructure facilities have had a substantial influence on the increasing pattern of urbanization within the concerned period. This is supported by the rising demographic data observed in the Galle MC area between 1996 and 2022. This is further supported by the growth in the population of the Galle urban area, which has risen from 86,568 in 1996 to a subsequent increase of 109,695 in 2022 (Department of Census and Statistics, 2023).

4.3 Policy implications to minimize UHI effect and EC

In light of the impervious surface expansion with decreasing green surface pattern and tendency, city planning agencies such as the Urban Development Authority (UDA) and MC should adopt sustainable city planning strategies, such as the implementation of green concepts in urban planning as suggested by other scholars (Senanayake et al., 2013; Ranagalage et al., 2017; Dissanayake, 2020). These strategies may include the establishment of green belts and the promotion of urban agriculture since the green surface has a cooling effect on LST due to its ability to generate cool island effects through evapotranspiration (Ranagalage et al., 2017; Dissanayake, 2020). These measures would be essentially in the high LST and UHI intensity hot spot areas including along busy roads and other dense settlement zones in and around the city core within $URGZ_{1-9}$ identified as in (Figure 8). Since transportation networks have greatly affected compacted urban growth, the liner green belts beside the roads will be more effective in reducing the effect of heat emitted from automobiles.

4.4 Limitations and future research directions

Though this research focused on quantifying the linear relationship between LST and impervious surface expansion,

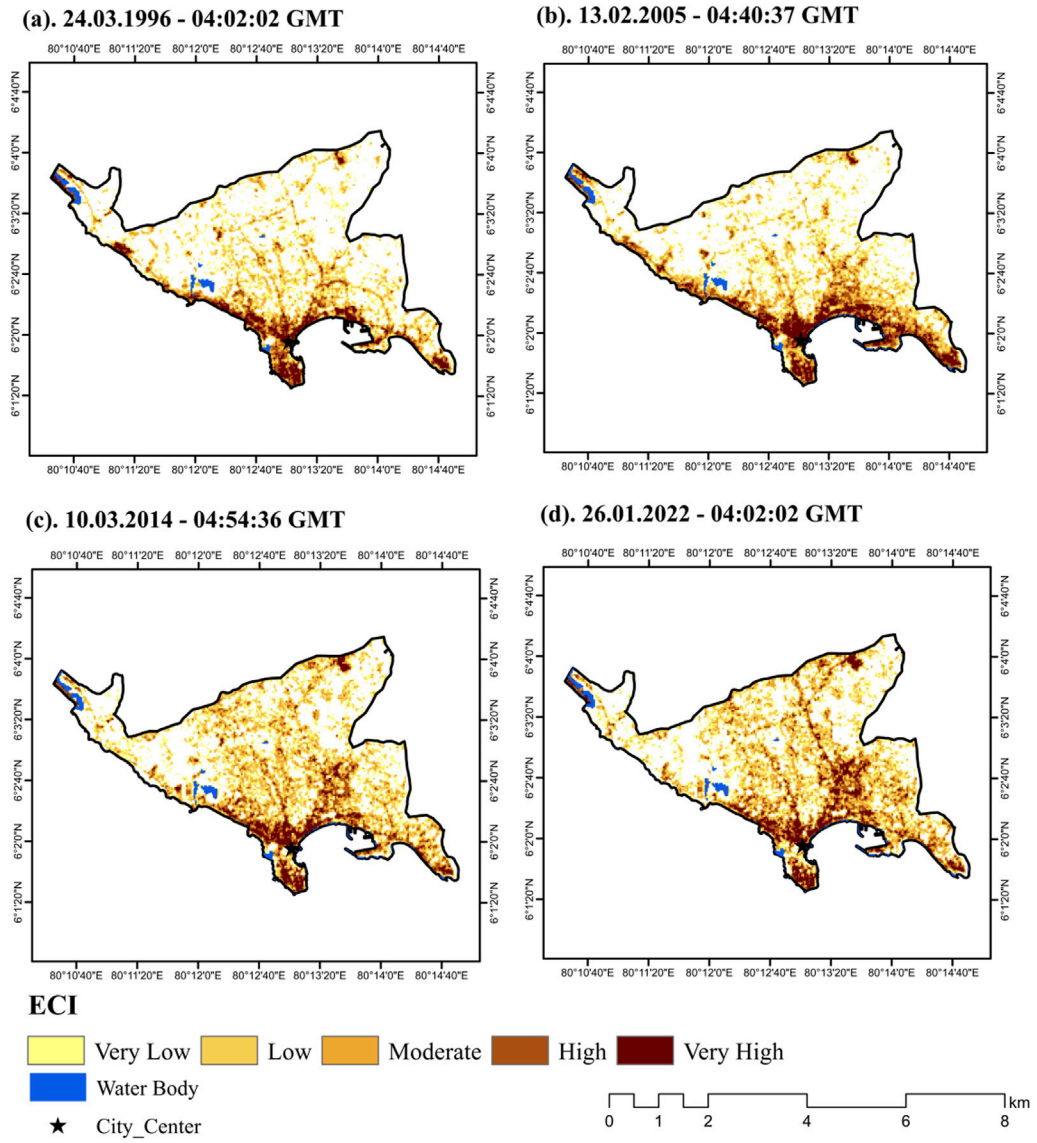

FIGURE 12
Environmental Criticality Index in Galle MC: **(A)** 1996; **(B)** 2005 **(C)** 2014; **(D)** 2022 [Note: WB and GS were excluded].

further investigation is necessary to explore the nonlinear relationship between LST and impervious surface, as well as the inverse correlation between NDVI, NDBI, ECI, and urban growth. This analysis should be incorporated with additional data on precipitation and temperature, similar to the suggestions made by Fonseka et al. (2019). Due to time and resource constraints, we did not perform short-term (monthly/annual) trend analysis of UHI. However, to enhance the robustness and reliability of similar studies in the future, we recommend including short-term trend analysis. In future research, high-resolution thermal remote sensing images can be utilized to derive more precise LULC maps and other indices such as LST, NDVI, and NDBI, ensuring improved reliability by mitigating the impact of cloud cover, as observed in Landsat images. Additionally, those indices are not only reliant on the LULC classes as well other variables such as wind speed, solar radiation, and surface moisture, have an impact on the situation (Dissanayake et al., 2019). However, it is not feasible to measure such variables using Landsat data. Furthermore, the measurement of nighttime temperature using Landsat data was unattainable. Similar to the findings of (Dissanayake, 2020) it is crucial to do further research to determine if the Galle MC has reached its maximum capacity in terms of available land for new IS (Dissanayake, 2020).

5 Conclusion

Our study emphasized the spatial and temporal alterations in LST and UHI intensity linked to structural changes in the impervious surface in Galle MC. It highlighted that Galle MC experienced rapid impervious surface expansion over the 26 years while green surface showed a considerable decrease. The study specifically focused on the effect of impervious surface expansion upon LST and UHI intensity that occurred between 1996 and 2022,

utilizing Landsat data. The results found that the rapid expansion of impervious surface by 7.34 km^2 between 1996 and 2022 has significantly caused the decline of green surface and other LULC types. The study demonstrated that rapid urban growth extended into rural peripheries, and the FIS contributed to the rise in mean LST. This has led to an increase in LST, UHI, and the emergence of environmentally critical areas, in and around the Galle MC. The mean LST experienced a 2.7°C increase during 26 years. By 2022, the expanded impervious surface regions exhibit the highest concentrations of LST and EC, surpassing the conditions experienced in 1996. The regression results revealed that impervious surface expansion has a greater impact on LST since there is a strong positive correlation between NDBI and LST. Thus, green urban planning strategies are essential to minimize the adverse effects of UHI and environmental criticality in the study area, especially for identified UGZ. Land use planning and other related regulations should be updated considering the findings of these remote sensing-based biophysical indices. And also, this method can be applied to other Cities along with high-resolution satellite data and validation techniques. Due to very rare previous research, this study can be used as an urban planning road map that focuses on the green city concept and human security.

Data availability statement

The original contributions presented in the study are included in the article/Supplementary Material, further inquiries can be directed to the corresponding author.

Author contributions

DC: Conceptualization, Data curation, Formal Analysis, Investigation, Methodology, Resources, Software, Validation, Writing–original draft. NW: Conceptualization, Data curation, Formal Analysis, Investigation, Methodology, Resources, Software, Validation, Writing–original draft. PM: Data curation, Methodology, Resources, Writing–review and editing. WF: Formal Analysis, Investigation, Methodology, Resources, Validation, Visualization, Writing–review and editing. KA: Funding acquisition, Project administration, Supervision, Visualization, Writing–review and editing. MF: Formal Analysis, Funding acquisition, Project administration, Supervision, Visualization, Writing–review and editing.

Funding

The author(s) declare that financial support was received for the research, authorship, and/or publication of this article. The authors express their profound appreciation to the Researchers Supporting Project number (RSP2025R351), King Saud University, Riyadh, Saudi Arabia, for providing financial support for this research work.

Acknowledgments

The authors would like to extend their gratitude to the reviewers and editors for their invaluable feedback, which significantly improved the quality of the manuscript. Additionally, we express our appreciation to the U.S. Geological Survey (USGS), NASA, and The University of Maryland for providing open-source Landsat data.

Conflict of interest

The authors declare that the research was conducted in the absence of any commercial or financial relationships that could be construed as a potential conflict of interest.

Publisher's note

Supplementary material

The Supplementary Material for this article can be found online at: https://www.frontiersin.org/articles/10.3389/fenvs.2024.1474742/full#supplementary-material

References

Abeyweera, M. A. N. S., and Kaluthanthri, P. C. (2018). "Attributes of city brand of Galle city, Sri Lanka," in *Proceedings of the international conference on real estate management and valuation (ICREMV)* (Sri Lanka: Colombo), 100–111.

Alqurashi, A. F., and Kumar, L. (2014). Land use and land cover change detection in the Saudi arabian desert cities of makkah and AlTaif using satellite data. *Adv. Remote Sens.* 3, 106–119. doi:10.4236/ars.2014.33009

Arachchi, M. A. S. M. M. (2022). Determination of urban heat island phenomena in a small-scale city, based on Landsat 8 data: a case study of Gampola urban area, Sri Lanka. *J. Trop. Env.* 2 (1).

Aubard, V., Paulo, J. A., and Silva, J. M. N. (2019). Long-term monitoring of cork and holm oak stands productivity in Portugal with Landsat imagery. *Remote Sens.* 11, 525. doi:10.3390/rs11050525

Bokaie, M., Zarkesh, M. K., Arasteh, P. D., and Hosseini, A. (2019). Assessment of urban heat island based on the relation-ship between land surface temperature and land use/land cover in Tehran. *Sus.Cities Soc.* 23, 94–104. doi:10.1016/j.scs.2016.03.009

Cabral, P., Feger, C., Levrel, H., Chambolle, M., and Basque, D. (2016). Assessing the impact of land-cover changes on ecosystem services: a first step toward integrative planning in Bordeaux, France. *Ecosys. Serv.* 22, 318–327. doi:10.1016/j.ecoser.2016.08.005

Chatterjee, U., and Majumdar, S. (2022). Impact of land use change and rapid urbanization on urban heat island in Kolkata city: a remote sensing based perspective. *J. Urban Mang.* 11, 59–71. doi:10.1016/j.jum.2021.09.002

Cheng, H., Deng, Q., Zhou, Z., Ren, Z., and Shan, X. (2022). Influence of land cover change on spatio-temporal distribution of urban heat island —a case in Wuhan main urban area. *Cities Soci.* 79, 103715. doi:10.1016/j.scs.2022.103715

Choe, Y. J., and Yom, J. H. (2020). Improving accuracy of land surface temperature prediction model based on deep-learning. *Sp. Info. Res.* 28, 377–382. doi:10.1007/s41324-019-00299-5

Congalton, R. G. (1991). A review of assessing the accuracy of classifications of remotely sensed data. *Remote Sens. Envir.* 37, 35–46. doi:10.1016/0034-4257(91)90048-B

Deng, Y., Zhang, L., Hao, L., Sun, G., Liu, Y., and Zhu, C. (2016). Spatiotemporal trends of urban heat island effect along the urban development intensity gradient in China. *Habitat Int.* 544, 617–626. doi:10.1016/j.scitotenv.2015.11.168

Department of Census and Statistics (2023). District statistical handbook. *Galle*. Available at: http://www.statistics.gov.lk/ref/HandbookDictionary#gsc.tab=0.

Dissanayake, D., Morimoto, T., Ranagalage, M., and Murayama, Y. (2019). Land-use/land-cover changes and their impact on surface urban heat islands: case study of Kandy city, Sri Lanka. *Climate* 7 (99), 1–20. doi:10.3390/cli7080099

Dissanayake, D. M. S. L. B. (2020). Land use change and its impacts on land surface temperature in Galle city, Sri Lanka. *Climate* 8, 65. doi:10.3390/cli8050065

Environmental Protection Agency (2008). *Reducing urban heat islands: compendium of strategies urban heat island basics*. Washington, DC, USA: EPA.

Estoque, R. C., and Murayama, Y. (2017). Monitoring surface urban heat island formation in a tropical mountain cityusing Landsat data (1987–2015). *ISPRS J. Photo. Remote Sens.* 133, 18–29. doi:10.1016/j.isprsjprs.2017.09.008

Estoque, R. C., Murayama, Y., and Myint, S. W. (2017). Effects of landscape composition and pattern on land surface temperature: an urban heat island study in the megacities of Southeast Asia. *Sci. Envir.* 577, 349–359. doi:10.1016/j.scitotenv.2016.10.195

Fonseka, H. P. U., Zhang, H., Sun, Y., Su, H., Lin, H., and Lin, Y. (2019). Urbanization and its impacts on land surface temperature in Colombo metropolitan area, Sri Lanka, from 1988 to 2016. *Remote Sens.* 11, 957. doi:10.3390/rs11080957

Ho, H. C., Knudby, A., Xu, Y., Hodul, M., and Aminipouri, M. (2016). A comparison of urban heat islands mapped using skin temperature, air temperature, and apparent temperature (Humidex), for the greater Vancouver area. *Sci. Envir.* 544, 929–938. doi:10.1016/j.scitotenv.2015.12.021

Hou, H., Wang, R., and Murayama, Y. (2019). Scenario-based modelling for urban sustainability focusing on changes in cropland under rapid urbanization: a case study of Hangzhou from 1990 to 2035. *Sci. Environ.* 661, 422–431. doi:10.1016/j.scitotenv.2019.01.208

Ishtiaque, A., Shrestha, M., and Chhetri, N. (2017). Rapid urban growth in the Kathmandu valley, Nepal: monitoring land use land cover dynamics of a Himalayan city with Landsat imageries. *Environments* 4, 72. doi:10.3390/environments4040072

Jaafar, W. S., Abdul Maulud, K. N., Muhmad Kamarulzaman, A. M., Raihan, A., Md Sah, S., Ahmad, A., et al. (2020). The influence of deforestation on land surface temperature:A case study of perak and kedah, Malaysia. *Forests* 11 (6), 670. doi:10.3390/f11060670

Jain, S., Sannigrahi, S., Sen, S., Sandeep, B., Chakraborthi, S., and Rahmat, S. (2020). Urban heat island intensity and its mitigation strategies in the fast growing urban area. *J. urban mang.* 9 (1), 54–66. doi:10.1016/j.jum.2019.09.004

Jayasinghe, A. D. S., and Withanage, W. K. N. C. (2020). Geographical information system-based multi-criteria decision analysis of potato cultivation land suitability in Welimada divisional secretariat, Sri Lanka. *Potato J.* 47 (2), 126–134.

Kennedy, R. E., Yang, Z., Gorelick, N., Braaten, J., Cavalcante, L., Cohen, W. B., et al. (2018). Implementation of the LandTrendr algorithm on Google Earth engine. *Remote Sens.* 10, 691. doi:10.3390/rs10050691

Kimothi, S., Thapliyal, A., Gehlot, A., Aledaily, A. N., Gupta, A., Bilandi, N., et al. (2023). Spatio-temporal fluctuations analysis of land surface temperature (LST) using Remote Sensing data (LANDSAT TM5/8) and multifractal technique to characterize the urban heat Islands (UHIs). *Sus. Energy Techn. Asses.* 55, 102956. doi:10.1016/j.seta.2022.102956

Kumara, P. B. T. P. (2022). Socio-economic boom in southern province of Sri Lanka and the role of university of ruhuna. *J. Univ. Ruh.* 10 (1), 1–3. doi:10.4038/jur.v10i1.8003ISSN2659-2053

Land-resources (2023). United States geological Survey.Landsat missions: landsat science products. Available at: https://www.usgs.gov/land-resources/nli/landsat/landsat-science-products (Accessed on November 12, 2023).

Landsat 8 (L8) (2016). *Data users handbook; version 2*, Vol. 8. USA: United States Geological Survey: Sioux Falls, SD.

Li, Z., Tang, B.-H., Wu, H., Ren, H., Yan, G., Wan, Z., et al. (2013). Satellite-derived land surface temperature: current status and perspectives. *Remote Sens. Envir.* 131, 14–37. doi:10.1016/j.rse.2012.12.008

Liu, Y., Wang, Y., Peng, J., Du, Y., Liu, X., Li, S., et al. (2015). Correlations between urbanization and vegetation degradation across the world's metropolises using DMSP/OLS nighttime light data. *Remote Sens.* 7, 2067–2088. doi:10.3390/rs70202067

Marconcini, M., Metz, A., Esch, T., and Zeidler, J. (2014). "Global urban growth monitoring by means of SAR data," in Proceedings of the 2014 IEEE Geoscience and Remote Sensing Symposium, Quebec City, QC, Canada, 13-18 July 2014, 1477–1480. doi:10.1109/igarss.2014.6946716

Mirzaei, P. A. (2015). Recent challenges in modeling of urban heat island. *Sus. Cities Soci.* 19, 200–206. doi:10.1016/j.scs.2015.04.001

Mohajane, M., Essahlaoui, A. L. I., Oudija, F., el Hafyani, M., El Hmaidi, A., Ouali, A., et al. (2018). Land use/land cover (LULC) using landsat data series (MSS, TM, ETM+ and OLI) in azrou forest, in the central middle atlas of Morocco. *Environments* 5, 131. doi:10.3390/environments5120131

Myint, S. W., Brazel, A., Okin, G., and Buyantuyev, A. (2010). Combined effects of impervious surface and vegetation cover on air temperature variations in a rapidly expanding desert city. *GIScience Remote Sens.* 47, 301–320. doi:10.2747/1548-1603.47.3.301

Nuwanka, M. W. R., and Withanage, W. K. N. C. (2024). A GIS-based framework for flood hazard vulnerability evaluation in Thudawa area, Sri Lanka. *Inte. J. Info. Deci. Sci.* 16 (1), 90–108. doi:10.1504/IJIDS.2024.10061741

Pannell, C. W. (2002). China's continuing urban transition. *Envir. Plann.* 34, 1571–1589. doi:10.1068/a34201

Paranunzio, R., Ceola, S., Laio, F., and Montanari, A. (2019). Evaluating the effects of urbanization evolution on air temperature trends using nightlight satellite data. *Atmosphere* 10, 117. doi:10.3390/atmos10030117

Priyankara, P., Ranagalage, M., Disanayake, D. M. S. L. B., Morimoto, T., and Murayama, Y. (2019). Spatial process of surface urban heat island in rapidly growing seoul metropolitan area for sustainable urban planning using landsat data (1996–2017). *Climate* 7, 110. doi:10.3390/cli7090110

Ranagalage, M., Dissanayake, D., Murayama, Y., Zhang, X., Estoque, R. C., Perera, E., et al. (2018a). Quantifying surface urban heat island formation in the world heritage tropical mountain city of Sri Lanka. *ISPRS Inte. J. Geo-Info.* 7, 341. doi:10.3390/ijgi7090341

Ranagalage, M., Estoque, R. C., Handayani, H. H., Zhang, X., Morimoto, T., Tadono, T., et al. (2018b). Relation between urban volume and land surface temperature: a comparative study of planned and traditional cities in Japan. *Sustainability* 10, 2366. doi:10.3390/su10072366

Ranagalage, M., Estoque, R. C., and Murayama, Y. (2017). An urban heat island study of the Colombo metropolitan area, Sri Lanka, based on landsat data (1997–2017). *ISPRS Inte. J. Geo-info.* 6, 189. doi:10.3390/ijgi6070189

Ranagalage, M., Murayama, Y., Dissanayake, D. M. S. L. B., and Simwanda, M. (2019). The impacts of landscape changes on annual mean land surface temperature in the tropical mountain city of Sri Lanka: a case study of Nuwara Eliya (1996-2017). *Sustainability* 11, 5517. doi:10.3390/su11195517

Ranagalage, M., Ratnayake, S. S., Dissanayake, D., Kumar, L., Wickremasinghe, H., Vidanagama, J., et al. (2020). Spatiotemporal variation of urban heat islands for implementing Na-ture-Based solutions: a case study of Kurunegala, Sri Lanka. *ISPRS Inte. J. Geo-info.* 9, 461. doi:10.3390/ijgi9070461

Rashid, N., Alam, J. A. M. M., Chowdhury, A., and Islam, S. L. U. (2022). Impact of land use change and urbanization on urban heat island effect in Narayanganj city, Bangladesh: a remote sensing-based estimation. *Envir. Chall.* 8, 1–11. doi:10.1016/j.envc.2022.100571

Rawat, J. S., and Kumar, M. (2015). Monitoring land use/cover change using remote sensing and GIS techniques: a case study of Hawalbagh block, district Almora, Uttarakhand, India. *Remote Sens. Space Sci.* 18, 77–84. doi:10.1016/j.ejrs.2015.02.002

Rimal, B., Zhang, L., Keshtkar, H., Wang, N., and Lin, Y. (2017). Monitoring and modeling of spatiotemporal urban ex-pansion and land-use/land-cover change using integrated Markov chain cellular automata model. *ISPRS Inte. J. Geo-Info.* 6, 288. doi:10.3390/ijgi6090288

Santos, A. R. D., Santos, D. O. F., Gomes, D. S. A., Gleriani, J. M., Goncalves, W., Moreira, G. L., et al. (2017). Spatial and temporal distribution of urban heat islands. *Sci. Envir.* 605–606, 946–956. doi:10.1016/j.scitotenv.2017.05.275

Sapena, M., and Ruiz, L. A. (2015). "Analysis of urban development by means of multi-temporal fragmentation metrics from lulc data," in *The international archives of the photogrammetry, remote sensing and spatial information Sciences, volume XL-7/W3, 2015 36th international symposium on remote sensing of environment* (Berlin, Germany), 11–15. doi:10.5194/isprsarchives-XL-7-W3-1411-2015

Saputra, L. I. A., Jumadi, A., and Sari, D. N. (2023). Analysis of environmental criticality index (ECI) and distribution of slums in yogyakarta and surrounding areas using multitemporal landsat imagery. *Proc. Int. Conf. Geogr. Disaster Manag.*, 407–420. doi:10.2991/978-2-38476-066-4_26

Senanayake, I. P., Welivitiya, W. D. D. P., and Nadeeka, P. M. (2013). Remote sensing based analysis of urban heat islands with vegetation cover in Colombo city. *Sri Lanka using Landsat-7 ETM+ data. Urban Cli* 5, 1935. doi:10.1016/j.uclim.2013.07.004

Shikary, C., and Rudra, S. (2020). Measuring urban land use change and sprawl using geospatial techniques: a study on purulia municipality, West Bengal, India. J. Indian soci. *Remote Sens.* 48 (11), 1–16.

Silva, J. S., Silva, R. M., and Santos, C. A. G. (2018). Spatiotemporal impact of land use/land cover changes on urban heat islands: a case study of Paço do Lumiar, Brazil. *Braz. Buil. Envi.* 136, 279–292. doi:10.1016/j.buildenv.2018.03.041

Son, N. T., Chen, C. F., Chen, C. R., Thanh, B. X., and Vuong, T. H. (2017). Assessment of urbanization and urban heatislands in Ho chi minh city, vietnam using landsat data. *Sustain. Cities Soc.* 30, 150–161. doi:10.1016/j.scs.2017.01.009

Sultana, S., and Satyanarayana, A. N. V. (2018). Urban heat island intensity during winter over metropolitan cities of India using remote-sensing techniques: impact of urbanization. *Inte. J. Remote Sens.* 39, 6692–6730. doi:10.1080/01431161.2018.1466072

Sultana, S., and Satyanarayana, A. N. V. (2020). Assessment of urbanisation and urban heatisland intensities using landsat imageries during 2000 – 2018 over a subtropical Indian City. *Sustain Cities Soc.* 52, 101846. doi:10.1016/j.scs.2019.101846

Teferi, E., and Abraha, H. (2017). "Urban heat island effect of Addis Ababa City: implications of urban green spaces for climate change adaptation," in *Climate change adaptation in africa* (Berlin, Germany: Springer).

Tepanosyan, G., Muradyan, V., Hovsepyan, A., Pinigin, G., Medvedev, A., and Asmaryan, S. (2021). Studying spatial-temporal changes and relationship of land cover and surface Urban Heat Island derived through remote sensing in Yerevan, Armenia. *Buil. Envio.* 187, 107390. doi:10.1016/j.buildenv.2020.107390

Tian, Y., Shuai, Y., Ma, X., Shao, C., Liu, T., and Tuerhanjiang, L. (2022). Improved landscape expansion index and its application to urban growth in urumqi. *Remote Sens.* 14, 5255. doi:10.3390/rs14205255

United Nations, Department of Economic and Social Affairs, Population Division. (2019). World urbanization prospects 2018: highlights (ST/ESA/SER.A/421).

United States Geological Survey (2018). *Product guide: Landsat 8 surface reflectance code (LASRC) product; depart-ment of the interior*. USA: U.S. Geological Survey: Sioux Falls, SD.

United States Geological Survey (2020). *Landsat 4–7 collection 1 (C1) surface reflectance (LEDAPS) product guide; department of the interior*. USA: U.S. Geological Survey: Sioux Falls, SD.

Urban Development Authority (2019). *Development plan for greater Galle area 2019–2030, Part I; urban development authority: Galle*. Sri Lanka.

Wang, J., Kuffer, M., and Pfeffer, K. (2019). The role of spatial heterogeneity in detecting urban slums. *Com. Envir. Urban Sys.* 73, 95–107. doi:10.1016/j.compenvurbsys.2018.08.007

Wanga, W., Liua, K., Tangb, R., and Wangc, S. (2019). Remote sensing image-based analysis of the urban heat island effect in Shenzhen, China. Phy. *Chem. Earth.* 110, 168–217. doi:10.1016/j.pce.2019.01.002

Weng, Q. (2002). Land use change analysis in the Zhujiang Delta of China using satellite remote sensing, GIS and stochastic modelling. *J. Envir. Manag.* 64, 273–284. doi:10.1006/jema.2001.0509

Weng, Q. (2009). Thermal infrared remote sensing for urban climate and environmental studies: methods, applications, and trends. *ISPRS J. Photo. Remote Sens.* 64, 335–344. doi:10.1016/j.isprsjprs.2009.03.007

Wijesinghe, D. C., Mishra, P. K., Withanage, N. C., Abdelrahman, K., Mishra, V., Tripathi, S., et al. (2023). Application of GIS, multi-criteria decision-making techniques for mapping groundwater potential zones: a case study of thalawa division, Sri Lanka. *Water* 15 (19), 3462. doi:10.3390/w15193462

Wijesinghe, W. M. D. C., and Withanage, W. K. N. C. (2021). Detection of the changes of land use and land cover using remote sensing and GIS in Thalawa DS Division. *Prathimana J.* 14 (1), 72–86.

Wijesinghe, W. M. D. C., Withanage, W. K. N. C., Mishra, P. K., Ranagalage, M., Abdelrahman, K., and Fnais, M. S. (2024). An application of the remote sensing derived indices for drought monitoring in a dry zone district, in tropical island. *Ecol. Indi* 167 (112681), 1–20. doi:10.1016/j.ecolind.2024.112681

Wimalasena, K. H. M. D. P., and Withanage, W. K. N. C. (2022). A GIS-based spatial variations analysis of water quality in domestic wells in the buttala area, Sri Lanka. *J. Soc. Sci. Huma. Revi.* 6 (3), 155–169. doi:10.4038/jsshr.v6i3.64

Withanage, N. C., and Jingwei, S. (2024). Evaluating the spatial-temporal dynamics of urbanization in prefecture cities of China using SNPP-viirs nighttime light remote sensing data. *Gazi Univ. J. Sci. Part A Eng. Inno.* 11 (2), 346–371. doi:10.54287/gujsa.1466745

Withanage, N. C., Wijesinghe, D. C., Mishra, P. K., Abdelrahman, K., Mishra, V., and Fnais, M. S. (2024). An ecotourism suitability index for a world heritage city using GIS-multi criteria decision analysis techniques, Sri Lanka. *Heliyon* 10 (2024), 1–16. doi:10.1016/j.heliyon.2024.e31585

Withanage, W. K., Mishra, P. K., and Jayasinghe, B. C. (2024). An assessment of spatio-temporal land use/land cover dynamics using landsat time series data (2008-2022) in kuliyapitiya west divisional secretariat division in kurunagala district, Sri Lanka. *J. Geosp. Surv.* 4 (1), 12–23. doi:10.4038/jgs.v4i1.52

Withanage, N. C., Shi, K., and Shen, J. (2023). Extracting and evaluating urban entities in China from 2000 to 2020 based on SNPP-VIIRS-like data. *Remote Sens.* 15, 4632. doi:10.3390/rs15184632

Withanage, W. K., Gunathilaka, M. D. K. L., Mishra, P. K., Wijesinghe, W. M. D. C., and Tripathi, S. (2023). Indexing habitat suitability and human-elephant conflicts using GIS-MCDA in a human-dominated landscape. *Geo. Sust.* 4 (4), 343–355. doi:10.1016/j.geosus.2023.08.004

Wu, C., and Murray, A. T. (2003). Estimating impervious surface distribution by spectral mixture analysis. *Remote Sens. Envir.* 84, 493–505. doi:10.1016/S0034-4257(02)00136-0

Xiao, H., and Weng, Q. (2007). The impact of land use and land cover changes on land surface temperature in a karst area of China. *J. Envir. Manag.* 85 (1), 245–257. doi:10.1016/j.jenvman.2006.07.016

Xu, L. Y., Xie, X. D., and Li, S. (2013). Correlation analysis of the urban heat island effect and the spatial and temporal distribution of atmospheric particulates using TM images in Beijing. *Envir. Poll.* 178, 102–114. doi:10.1016/j.envpol.2013.03.006

Ziaul, S., and Pal, S. (2016). Image-based surface temperature extraction and trend detection in an urban area of West Bengal, India. *J. Envir. Geo.* 9, 13–25. doi:10.1515/jengeo-2016-0008